OPEN ACCESS

Energetic Evaluation and Optimization of Hydrogen Generation and Compression Pathways Considering PEM Water Electrolyzers and Electrochemical Hydrogen Compressors

To cite this article: Lars Zachert *et al* 2021 *J. Electrochem. Soc.* **168** 014504

Journal of The Electrochemical Society, 2021 **168** 014504

Energetic Evaluation and Optimization of Hydrogen Generation and Compression Pathways Considering PEM Water Electrolyzers and Electrochemical Hydrogen Compressors

Lars Zachert, Michel Suermann, Boris Bensmann,[z] and Richard Hanke-Rauschenbach

Institute of Electric Power Systems, Leibniz Universität Hannover, 30167 Hannover, Germany

Electrochemical hydrogen compression is seen as a promising alternative to mechanical compression in the context of power-to-gas plants. It can be carried out either as direct co-compression in a water electrolyzer (WE) or via a separate electrochemical hydrogen compressor (EHC). This study analyzes the specific energy demand of different hydrogen generation and compression pathways using WEs and EHCs, both based on proton exchange membrane (PEM) technology, for pressures up to 1000 bar. The energy demand is systematically investigated as a function of design parameters such as pressure, current density, temperature and membrane thickness and presented in overpotential-specific and gas-crossover dependent shares. The analysis reveals intrinsic differences in the compression behavior of WEs and EHCs. In the EHC, permeated hydrogen is simply re-compressed back to the cathode. In the WE, instead, water has to be split again to compensate for the hydrogen loss, causing energetic disadvantages with increasing hydrogen pressure. Moreover, using an EHC enables design parameters to be optimized separately regarding hydrogen generation and compression. Therefore, at low current densities, compression via EHC is already favorable to co-compression via WE for pressures above 4 bar. With increasing current density, however, this intersection point shifts up to pressures above 200 bar.

 [DOI: 10.1149/1945-7111/abcf1a]

Manuscript submitted July 20, 2020; revised manuscript received November 22, 2020. Published January 7, 2021.

Supplementary material for this article is available online

List of symbols

a_i	activity of species i / -
D_i	diffusion coefficient of species i / $m^2\ s^{-1}$
E	cell voltage / V
E_0	thermodynamic cell voltage / V
f_i	fugacity of species i / Pa
F	Faraday constant / 96485.33 A s mol^{-1}
ΔG	molar change in Gibbs free energy / J mol^{-1}
i	current density / A m^{-2}
i_0	apparent exchange current density / A m^{-2}
$k_{L,i}$	mass transfer coefficient of species i / m s^{-1}
M_i	molar mass of species i / g mol^{-1}
N_i	molar flux of species i / mol $m^{-2}\ s^{-1}$
p	absolute pressure / Pa
p_{ref}	reference pressure / Pa
p_i	partial pressure of species i / Pa
R	ohmic area resistance / $\Omega\ m^2$
R	molar gas constant / 8.314 J $mol^{-1}\ K^{-1}$
S_i	solubility of species i / mol $m^{-3}\ Pa^{-1}$
T	temperature / K
V_i	Volume of species i / m^3
w	energy demand / kWh kg_{H2}^{-1}
Z_i	compressibility factor of species i / -
$\overleftarrow{\alpha}$	transfer coefficient of the oxidation reaction / -
$\overrightarrow{\alpha}$	transfer coefficient of the reduction reaction / -
δ	thickness / m
ϵ	porosity / -
η	overpotential / V
θ	ratio of hydrogen output at the cathode to the total amount of electrochemically produced hydrogen / -
λ	water content / S m^{-1}
σ	proton conductivity / $mol_{H2O}\ mol_{SO3H}^{-1}$
τ	geometric tortuosity / -
ϕ_i	fugacity coefficient of species i / -

Subscripts and superscripts

a	anode
act	activation
c	cathode
ch	channel
cl	catalyst layer
conc	concentration
del	delivery
dis	dissolved phase
eff	effective
EHC	electrochemical hydrogen compressor
el	electrical
evo	evolution
gas	gaseous phase
H2	hydrogen
H2O	water
in	inlet
m	membrane
min	minimum
O2	oxygen
out	outlet
oxi	oxidation
perm	permeation
ref	reference
s	specific
sat	saturated
WE	water electrolyzer

An increasing share of renewable energy production in the European electricity sector (32.1 % in 2018[1]) raises the need for efficient energy storage concepts to store the intermittent power generation from wind and solar power plants.[2] Green hydrogen as an energy carrier, which can either be re-electrified or used to transfer renewable energy into other sectors, can help tackle this dilemma. For large-scale production of green hydrogen with an intermittent power supply, low-temperature water electrolysis looks promising compared to alternative technologies, such as high-temperature water electrolysis or photocatalytic water splitting.[3,4] Among the

[z]E-mail: boris.bensmann@ifes.uni-hannover.de

low-temperature water electrolysis technologies, alkaline water electrolysis (AEL) and proton exchange membrane water electrolysis (PEMWE) are of great interest. While AEL is already relatively mature and available on a large scale, in combination with intermittent power supply PEMWE is rather preferred because of its dynamic properties and wide operating window.[3]

Depending on the application, hydrogen is typically required at elevated pressure levels for efficient storage and transportation. A hydrogen pressure of 200 bar, for example, is used for long-term high-capacity storage in salt caverns, hydrogen transportation in trucks, and industrial processes such as ammonia production and iron reduction. Hydrogen refueling stations (HFS) for automotive applications and other short-term storage tanks, on the other hand, can require hydrogen pressures of 800 bar or even higher.[5]

Usually, hydrogen is compressed to the required delivery pressure via conventional mechanical piston compressors or ionic liquid compressors.[6] Alternatively, hydrogen can be compressed electrochemically in an electrochemical hydrogen compressor (EHC) or directly in a water electrolyzer (WE) with the latter option being referred to as co-compression. Both AEL and PEMWE allow for balanced co-compression, operating at the same cathode and anode pressure. However, thanks to the solid electrolyte, PEMWE also allows for differential pressure operation with a pressure difference between the cathode and anode. In this work, only differential pressure operation is considered, limiting the scope of this paper to PEMWE. Using a WE, hydrogen differential pressures up to 700 bar [7] have been demonstrated, compared to 1000 bar using an EHC.[8] The advantages of electrochemical hydrogen compression over mechanical compression are, in particular, lower maintenance requirements and a noiseless, vibration-free operation due to the lack of moving parts.[9] Also, from a theoretical point of view, nearly isothermal electrochemical compression is preferable to isentropic mechanical compression. For real systems, however, major drawbacks of electrochemical hydrogen compression are the permeation of compressed hydrogen through the membrane from the cathode to the anode and the ohmic resistance of the membrane. Therefore, efficiency concerns as well as safety concerns regarding the hydrogen concentration at the WE anode have to be considered. Different mitigation strategies exist that reduce the gas-crossover itself, e.g. by using reinforced membranes, or reduce the H_2 in O_2 content at the anode, e.g. by implementing recombining catalysts.[10]

In the literature, different studies discuss the configuration of hydrogen generation and compression (hereinafter referred as production) pathways considering mechanical compressors.[5,11] There is, however, a lack of research on the optimal system design considering solely electrochemical hydrogen compression. Moreover, the general behavior of high pressure WEs and EHCs is investigated in the literature (e.g. Refs. 7, 12–14), whereas, to our knowledge, no such detailed energetic comparison of the two devices has been reported yet.

The present contribution gives a detailed, model-based analysis of electrochemical hydrogen production using high pressure WEs and EHCs. The study energetically evaluates and optimizes the two hydrogen production pathways (PW) that consider both electrochemical hydrogen generation and compression as sketched in Fig. 1a. PW I considers hydrogen generation (including co-compression) via WE and downstream compression to delivery pressure via EHC, whereas in PW II, hydrogen is generated and compressed to delivery pressure solely via WE. First, a detailed parameter study regarding important design parameters (pressure, current density, temperature and membrane thickness) is presented for the WE and the EHC. The specific energy demand in terms of the electrical energy required for producing one kilogram of hydrogen output (hereinafter referred to simply as energy demand) is divided into the reversible energy demand, losses associated with the individual overpotentials and gas-crossover losses to allow for a fundamental understanding of the dependencies. Similarities and differences between the WE and EHC are highlighted and discussed. Afterwards, the two hydrogen production pathways of interest are compared for hydrogen delivery pressures in the range of 1–1000 bar and the minimum energy demand of both pathways is shown as a function of the delivery pressure and current density. Two hydrogen delivery pressures, 200 bar and 800 bar, are chosen exemplarily to present the energetically optimal system configuration of both pathways regarding the aforementioned design parameters. The results show how to minimize the energetic cost, and thus the operating cost, of pressurized hydrogen supply while using WEs and/or EHCs. Finally, the resulting system configurations are critically discussed concerning real hydrogen production systems and development goals of high pressure WEs and EHCs.

Theory and Model Description

This section describes the general working principle of the WE and EHC and introduces the associated models used in this work. A detailed description of the models is given in the appendix (Eqs. A·1–A·27). A schematic illustration of a WE and an EHC cell, as well as the main mass transfer inside the cells is shown in Fig. 1b. The WE uses electrical energy to split water into oxygen, protons and electrons at the anode. Accompanied by a water flux, protons are conducted through a solid membrane and reduced to hydrogen at the cathode. The adjusted cathode channel pressure thereby determines the hydrogen outlet pressure. The EHC also sends protons through a solid membrane and reduces them back to hydrogen at a chosen cathode pressure. Unlike the WE, however, the EHC only compresses hydrogen rather than producing it. As the membrane is not completely impermeable for gases, both devices suffer from gas-crossover. Driven by a concentration gradient across the membrane, product gas permeates through the electrolyte reducing the efficiency. In the WE, permeated hydrogen from the cathode to the anode either recombines with evolved oxygen back to water or leaves the cell as an impurity in the oxygen gas. Contrary to this, in the EHC, permeated hydrogen is send back to the cathode, and compressed again.

Figure 1b also shows the associated system boundaries for the WE and EHC models, leaving peripheral consumers like transformers, water pumps, etc. out of consideration. Since this work focuses only on the production of hydrogen rather than oxygen, the energy demand of the WE and EHC is determined as the electrical energy demand normalized to the production and/or compression of one kilogram hydrogen at the respective device's cathode outlet. Thus, the total specific electrical energy demand of both the WE and the EHC is defined by Eq. 1.

$$w_{\mathrm{el}} = \frac{E \cdot i}{N_{\mathrm{H2}}^{\mathrm{c,out}} \cdot \mathrm{M_{H2}}} \qquad [1]$$

Herein, E is the cell voltage of the WE or the EHC, i is the current density, $N_{\mathrm{H2}}^{\mathrm{c,out}}$ is the hydrogen flux at the respective cathode outlet and $\mathrm{M_{H2}}$ is the molar mass of hydrogen.

The cell voltage is described as the sum of the thermodynamic cell voltage under currentless conditions E_0 and the overpotentials η_{x}:

$$E = E_0 + \eta_{\mathrm{act}}^{\mathrm{a}} + \eta_{\mathrm{act}}^{\mathrm{c}} + \eta_{\mathrm{conc}} + \eta_{\mathrm{m}} + \eta_{\mathrm{el}} \qquad [2]$$

In Eq. 2, $\eta_{\mathrm{act}}^{\mathrm{a}}$ and $\eta_{\mathrm{act}}^{\mathrm{c}}$ are the anodic and cathodic activation overpotentials, respectively, η_{m} is the ionic ohmic overpotential, η_{conc} is the concentration overpotential and η_{el} is the electrical ohmic overpotential, with the last two comprising both anodic and cathodic overpotential. The temperature and pressure dependent thermodynamic cell voltage E_0 is determined by the Nernst equation. While the deviation from an ideal gas is considered for hydrogen using the compressibility factor approach, oxygen is assumed to behave as an ideal gas because it is kept at ambient pressure in all calculations.

The anodic activation overpotential $\eta_{\mathrm{act}}^{\mathrm{a}}$ belongs to the oxygen evolution reaction (OER) on iridium oxide in the WE and the hydrogen oxidation reaction (HOR) on platinum in the EHC. The

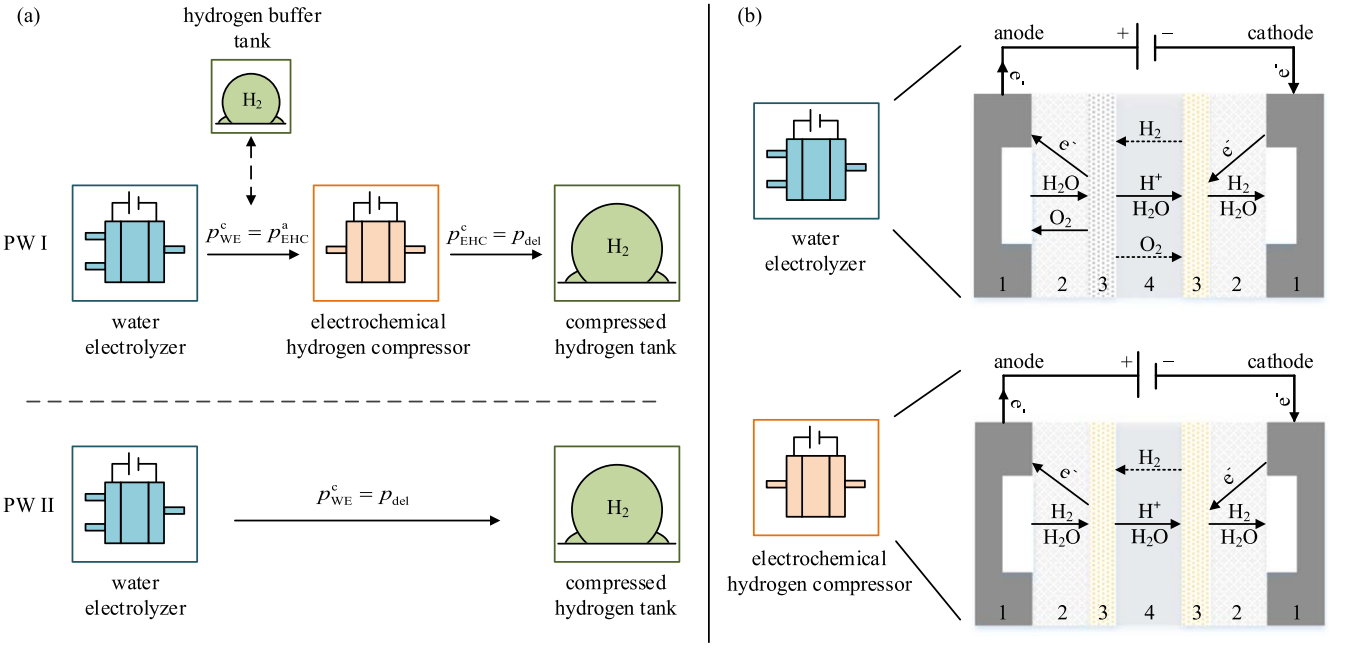

Figure 1. (a) Two hydrogen production pathways (PW) towards the desired delivery pressure p_{del} using WEs and EHCs. PW I: Hydrogen generation (including hydrogen co-compression up to a selected cathode pressure p_{WE}^{c}) via WE, and downstream further hydrogen compression from anode pressure $p_{EHC}^{a} = p_{WE}^{c}$ up to delivery pressure via EHC. Optional intermediate storage of hydrogen in a buffer tank between the WE and EHC. PW II: Hydrogen generation and direct hydrogen co-compression to delivery pressure via WE. (b) Schematic representation of the mass transfer inside WE and EHC cells and the main cell components, i.e. 1: bipolar plate with flow field, 2: porous transport layer, 3: catalyst layer, 4: membrane. The cells define the system boundaries used in this work, and thus the remaining components of a WE or EHC system are not considered. Also, the hydrogen tanks are not considered in the energetic analysis for the sake of simplicity.

cathodic activation overpotential η_{act}^{c}, on the other hand, belongs to the hydrogen evolution reaction (HER) on platinum in both the WE and the EHC. A Butler-Volmer approach is used to determine the activation overpotentials. The sluggish OER reaction kinetics result in significant overpotentials even at relatively small current densities, and thus the Butler-Volmer equation simplifies to the Tafel equation.[15] The overpotentials of the HER and HOR, on the contrary, are calculated using a linearized Butler-Volmer equation due to the fast reaction kinetics.[15,16]

The concentration overpotential η_{conc} is induced by concentration differences of the gases between the channel and the corresponding active side in the catalyst layer due to mass transport resistances. Water transfer to the reaction zone, however, is assumed to be ideal.

The ionic ohmic overpotential η_{m} describes the voltage increase due to proton transport through the membrane, considering the conductivity of a Nafion membrane for both devices.[17] The electrical ohmic overpotential η_{el} is induced by bulk and interfacial resistance between both electrodes. It is calculated based on an overall area-specific cell resistance that is considered temperature-independent, as the difference is negligibly small in the investigated temperature range between 20 °C and 80 °C.[18]

The cathodic hydrogen outlet flux $N_{H2}^{c,out}$ is determined by the following mass balance of hydrogen at the cathodic catalyst layer:

$$N_{H2}^{c,out} = N_{H2}^{evo} - N_{H2}^{perm} - 2 \cdot N_{O2}^{perm} \quad [3]$$

Here, N_{H2}^{evo} is the total amount of electrochemically evolved hydrogen at the cathode according to Faraday's law, that is $\frac{i}{2 \cdot F}$ with F as the Faraday constant. N_{H2}^{perm} is the hydrogen permeation flux from the cathode to the anode and N_{O2}^{perm} is the oxygen permeation flux from the anode to the cathode through the membrane. In the WE, it is assumed that permeated oxygen reacts with hydrogen back to water, and therefore reduces the hydrogen output at a stoichiometric ratio of 1:2. In the EHC, no oxygen is present, and thus the oxygen permeation flux is equal to zero. The permeation fluxes are calculated according to Fick's law of diffusion, considering also the concentration differences of the gases between the reaction zone and the channel.

In the following, the electrical energy demand in Eq. 1 is divided into the the energy demand without considering gas-crossover w_{el}^{evo}, and the gas-crossover losses w_{el}^{perm}:

$$w_{el} = \underbrace{\frac{E \cdot 2 \cdot F}{M_{H2}}}_{w_{el}^{evo}} + \underbrace{\frac{E \cdot 2 \cdot F}{M_{H2}} \cdot \frac{(1-\theta)}{\theta}}_{w_{el}^{perm}} \quad [4]$$

In Eq. 4, θ is the ratio of hydrogen output at the cathode to the total amount of electrochemically evolved hydrogen ($\theta = N_{H2}^{c,out}/N_{H2}^{evo}$). Hence, w_{el}^{evo} represents the energy required to produce and/or compress one kilogram of hydrogen at the reaction zone, and w_{el}^{perm} represents the energy required to produce and/or compress the additional hydrogen molecules that permeate through the membrane or react back to water with permeated oxygen.

Results

The results in this section are presented in four different paragraphs. At first, the WE and the EHC are introduced separately with a parameter analysis each. Afterwards, generic similarities and differences considering the compression behavior of the two hydrogen production pathways illustrated in Fig. 1a are pointed out. Finally, the energetically optimal system configuration is determined for both pathways.

Parameter study WE.—Starting with the WE, the influence of the following design parameters on the specific electrical energy demand is investigated: cathode pressure (p^{c} = 1–1000 bar), current density (i = 0.1–5 A cm^{-2}), temperature (T = 20–80 °C) and membrane thickness (δ_{m} = 20–300 μm). These parameters are chosen because they are adjustable for energetic reasons when designing a WE. The associated parameter ranges represent state of the art configurations and development goals of PEM WEs.[19,20] The anodic

electrolyzer pressure is not varied in this work, even if a slightly increased oxygen pressure, e.g. up to 10 bar, seems to further decrease the energy demand of the WE due to improved OER kinetics and reduced mass transport resistances.[12,13] Unfortunately, a proper model-theoretical description of this effect is still missing, and thus excluded here.

Figure 2 shows the electrical energy demand for producing one kilogram of hydrogen at the WE cathode outlet as a function of the aforementioned parameter variations, i.e. cathode pressure (Fig. 2a), current density (Fig. 2b), temperature (Fig. 2c) and membrane thickness (Fig. 2d). In each figure, the total electrical energy demand w_{el} is divided into two parts according to Eq. 4. The first part considers no permeation of product gases through the membrane and is illustrated with filled area colors that represent which share of the energy demand comes from the thermodynamic cell voltage E_0 and which shares come from the individual overpotentials η_x. The second part considers the gas-crossover losses w_{el}^{perm} and is illustrated with a hatched area. It should be noted that the gas-crossover losses are also directly linked to the separation made in Eq. 2, and hence can be attributed to either the thermodynamic cell voltage or the individual overpotentials.

While one parameter is varied, the remaining parameters are kept at reference conditions of $p^a = 1$ bar, $p^c = 200$ bar, $i = 1$ A cm^{-2}, $T = 20$ °C and $\delta_m = 150$ μm, with a corresponding energy demand of approximately 52 kWh kg$_{H2}^{-1}$. The selected reference membrane thickness corresponds to the fully swollen thickness of a Nafion 115 membrane. The following general observations can be made regarding all four parameter variations in Fig. 2:

- The largest proportion of the energy demand is attributed to the thermodynamic cell voltage, i.e. the reversible energy demand of the water splitting reaction, with approximately 32 kWh kg$_{H2}^{-1}$ at 60 °C and 1 bar.
- The second largest proportion of the energy demand is attributed to the OER overpotential η_{act}^a for a wide range of the selected parameters.
- The HER overpotential η_{act}^c and the concentration overpotential η_{conc} both have a minor impact on the total energy demand.
- The impact of gas-crossover strongly depends on the chosen parameter set as discussed below.

The influences of the varied parameters on the thermodynamic cell voltage, the individual overpotentials and the gas-crossover losses are summarized in Table I. With increasing cathode pressure (Fig. 2a), the energy demand rises continuously due to increasing reversible compression work and gas-crossover losses. Assuming a constant cell temperature, the reversible compression work of the WE is characterized by an isothermal behavior and is defined as the difference between the reversible energy demand at cathode pressure and the reversible energy demand at ambient pressure $(E_0(p^c) - E_0(1\,\text{bar}))$. The hydrogen permeation flux shows an approximately linear correlation to the cathode pressure according to Fick's law of diffusion, resulting in dominant gas-crossover losses at elevated cathode pressures. For

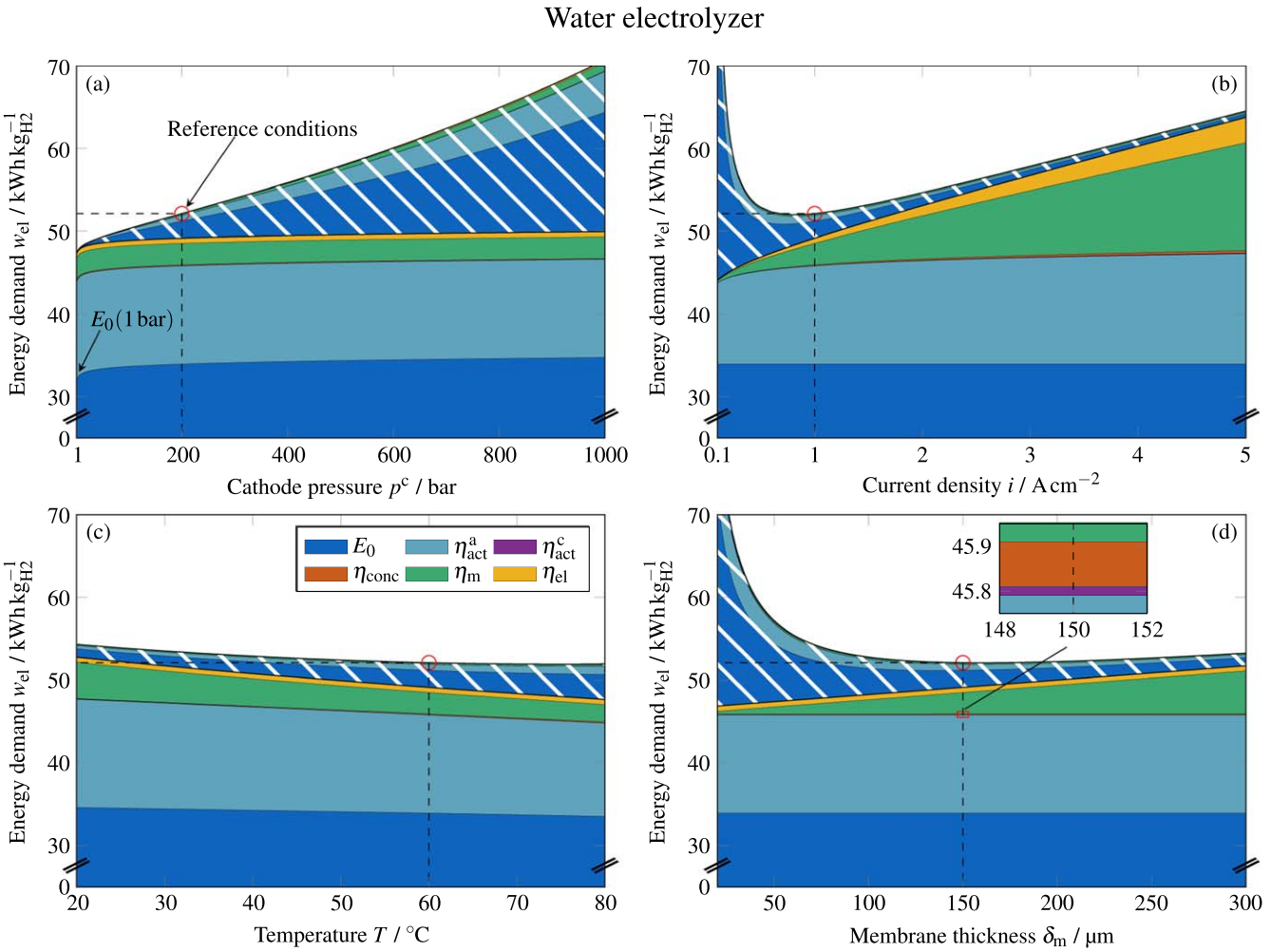

Figure 2. Electrical energy demand of hydrogen production via WE. The energy demand is divided into the thermodynamic cell voltage E_0, the individual overpotentials η_x and the gas-crossover losses w_{el}^{perm} (hatched area). The following parameters are varied in comparison to the reference conditions of $p^a = 1$ bar, $p^c = 200$ bar, $i = 1$ A cm^{-2}, $T = 60$ °C, $\delta_m = 150$ μm: (a) cathode pressure, (b) current density, (c) temperature, (d) membrane thickness.

Table I. Influence of increasing cathode pressure p^c, increasing current density i, increasing temperature T and increasing membrane thickness δ_m on the thermodynamic cell voltage E_0, the individual overpotentials η_x and the gas-crossover losses w_{el}^{perm} of the WE and EHC. All parameter dependencies are the same for the WE and EHC, except for the temperature dependence of the thermodynamic cell voltage. The temperature dependence of the electrical ohmic overpotential η_{el} is negligible in the investigated temperature range, and therefore not considered.

	p^c	i	T	δ_m
E_0	↗	—	↘ (WE) ↗ (EHC)	—
η_{act}^a	—	↗	↘	—
η_{act}^c	—	↗	↘	—
η_{conc}	↘	↗	↗	↗
η_m	—	↗	↘	↗
η_{el}	—	↗	(↗)	—
w_{el}^{perm}	↗	↘	↗	↘

instance, at a cathode pressure of 870 bar, the gas-crossover losses amount to a quarter of the total energy demand, i.e. for three molecules of hydrogen output, four molecules have to be electrochemically produced. Except for a slightly decreasing concentration overpotential with increasing cathode pressure, all other overpotentials are considered independent of pressure.

Figure 2b illustrates the impact of the current density on the WE energy demand. The energy demand is mostly determined by a trade-off between the gas-crossover losses and the ohmic overpotential losses. At current densities below 0.5 A cm^{-2}, the gas-crossover losses become more dominant because only small amounts of hydrogen are produced and the loss of product gas considerably decreases the hydrogen output at the cathode outlet. On the contrary, the impact of the gas-crossover losses on the total energy demand decreases for high current densities because the permeation flux plays a subsidiary role compared to the total amount of produced hydrogen. The ohmic overpotentials η_m and η_{el} as well as the HER activation potential η_{act}^c rise linearly with increasing current density according to ohm's law and the linearized Butler-Volmer equation, whereas the OER activation overpotential η_{act}^a shows a logarithmic dependence on the current density. Finally, the concentration overpotential also increases slightly with increasing current density because the concentration at the respective catalyst layer increases when more gas evolves.

In Fig. 2c, the temperature of the WE is varied between 20 °C and 80 °C. Except the electrical ohmic overpotential, for which a temperature dependence is negligibly small, the temperature affects each overpotential as well as the thermodynamic cell voltage and the gas-crossover. It can be noted that with increasing temperature (i) the thermodynamic cell voltage decreases slightly as a result of two opposing effects: While the reversible compression work increases, the change in Gibbs free energy of the water splitting reaction ΔG decreases, (ii) the activation overpotentials decrease due to improved reaction kinetics, (iii) the concentration overpotential increases because of the increased compression work that is needed to overcome the pressure gradient between catalyst layer and channel, (iv) the ionic ohmic overpotential decreases due to an increased proton conductivity of the membrane, and (v) the gas-crossover losses increase due to increasing diffusion coefficients of the dissolved gases in the membrane.

The variation of the membrane thickness (Fig. 2d) shows that, similar to the variation of the current density (Fig. 2b), a trade-off between the gas-crossover losses and the losses induced by the ionic ohmic overpotential determines the minimum energy demand. The gas-crossover losses strongly increase with decreasing membrane thickness due to the inversely proportional dependence, whereas the ohmic proton transport losses decrease in a linear fashion. In addition, the gas concentrations at the catalyst layer, and thus also the concentration overpotential, increase with increasing membrane thickness because less gas permeates through the membrane.

Parameter study EHC.—Analogous to the WE parameter study, the EHC characteristics are examined on the basis of Figs. 3a–3d. Reference conditions are again chosen as $p^a = 1$ bar, $p^c = 200$ bar, $i = 1$ A cm^{-2}, $T = 60$ °C, $\delta_m = 150$ μm, resulting in an energy demand of 5.7 kWh kg$_{H2}^{-1}$ for hydrogen compression. The findings of the EHC parameter study are described individually at first and then linked to the WE parameter study. With regard to the investigated parameter ranges, the following EHC properties can be obtained from Figs. 3a–3d:

- The thermodynamic cell voltage E_0, i.e. the reversible compression work, and the ionic ohmic overpotential η_m dominate the energy demand of the EHC for a wide range of the selected parameters.
- The HOR and the HER activation overpotentials η_{act}^a and η_{act}^c as well as the concentration overpotential η_{conc} have a minor impact on the energy demand.
- The impact of gas-crossover strongly depends on the chosen parameter set.

The influences of the parameter variations on the EHC energy demand are summarized in Table I as well. The energy demand of the EHC rises continuously with increasing cathode pressure (Fig. 3a) due to increasing compression work and increasing gas-crossover losses. The thermodynamic cell voltage E_0 is only determined by the reversible compression work, and thus equal to zero at ambient pressure operation. The concentration overpotential decreases slightly, whereas all other overpotentials are considered independent of cathode pressure.

In Fig. 3b, below the energetic optimum of approximately 0.3 A cm^{-2}, gas-crossover losses rise steeply due to the relatively small amounts of compressed hydrogen. With increasing current density, the ohmic overpotentials as well as the HER and HOR activation overpotential lead to a quasi-linear increase in energy demand. It should be noted that the energy demand induced by the ionic ohmic overpotential accounts for more than half of the total energy demand above approximately 1 A cm^{-2}, indicating that relatively thin membranes are energetically optimal for the EHC at elevated current densities compared to the reference membrane of 150 μm.

With increasing temperature (Fig. 3c), the reversible compression work E_0, the concentration overpotential and the gas-crossover losses of the EHC increase, whereas the activation overpotentials and the ionic ohmic overpotential decrease (for explanation see the evaluation of WE temperature dependencies regarding Fig. 2c).

The minimum energy demand in dependence of the membrane thickness (Fig. 3d) is determined by a trade-off between the gas-crossover losses and the losses induced by the ionic ohmic overpotential.

In comparison to the WE parameter study, the following generic similarities and differences between the WE and the EHC can be obtained. Comparing the variation of the cathode pressure in Figs. 2a and 3a, both devices require the same reversible compression work due to their isothermal compression behavior. One decisive difference between the devices is, however, that the gas-crossover losses of the WE show a significantly steeper slope with increasing cathode pressure. While in the WE another hydrogen molecule has to be produced for every permeated molecule, permeated hydrogen molecules in the EHC just have to be re-compressed. Therefore, only the energy that was expended for hydrogen compression rather than its generation accounts for the EHC gas-crossover losses. Consequently, the losses associated with gas-crossover are significantly higher for the WE than for the EHC, even though the hydrogen permeation flux in both devices is approximately the same.

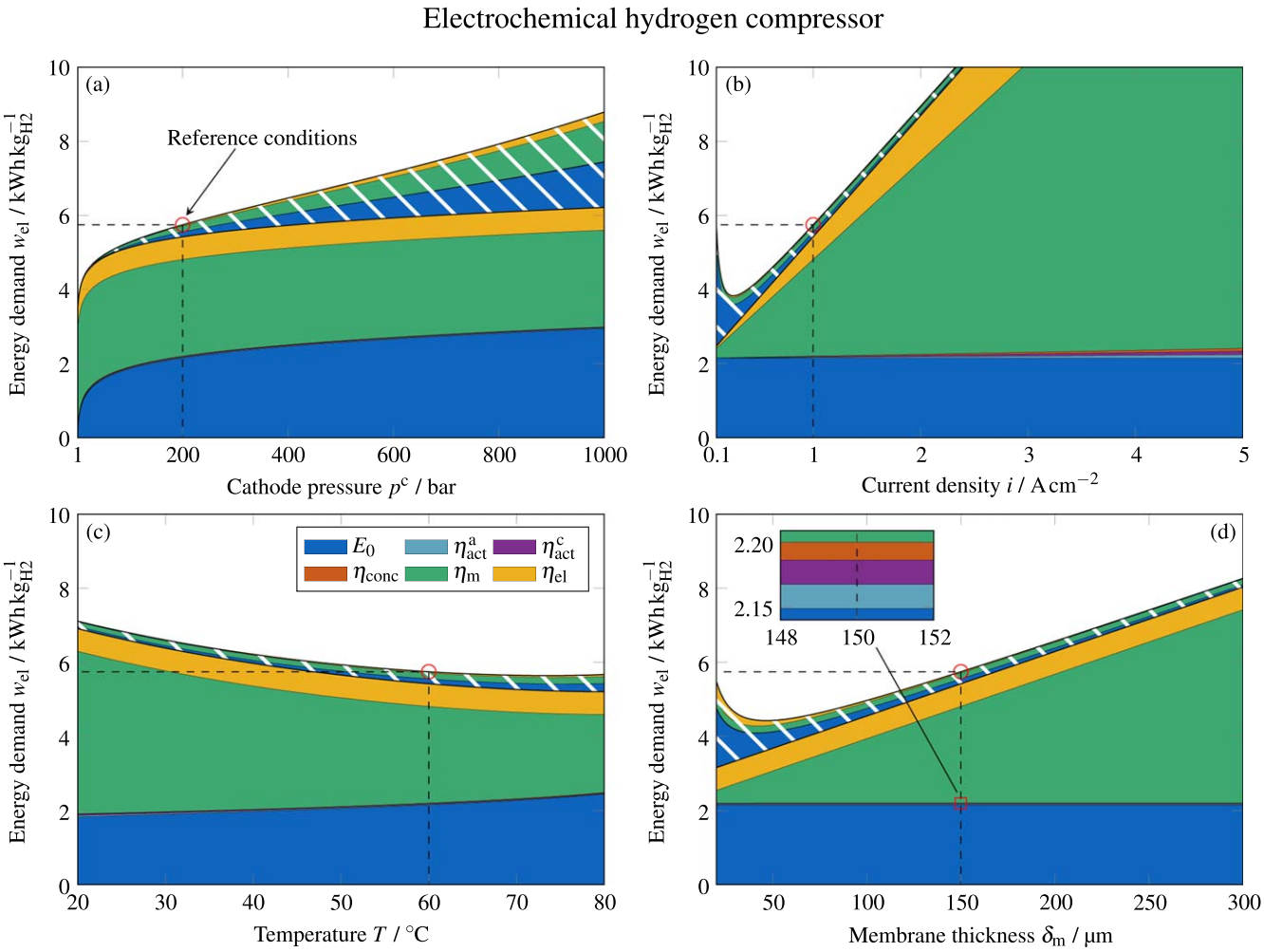

Figure 3. Electrical energy demand of hydrogen compression via EHC. The energy demand is divided into the thermodynamic cell voltage E_0, the individual overpotentials η_x and the gas-crossover losses w_{el}^{perm} (hatched area). The following parameters are varied in comparison to the reference conditions of $p^a = 1$ bar, $p^c = 200$ bar, $i = 1$ A cm^{-2}, $T = 60$ °C, $\delta_m = 150$ μm: (a) cathode pressure, (b) current density, (c) temperature, (d) membrane thickness.

Oxygen gas-crossover further increases that difference. This, however, is of minor relevance for the WE which operates at ambient pressure at the anode side.

Another key difference between the WE and EHC is the temperature dependence. While the isothermal compression work of both devices increases with increasing temperature, the change in Gibbs free energy of the water splitting reaction ΔG decreases only for the WE. Therefore, the thermodynamic cell voltage of the WE decreases with increasing temperature, whereas it increases for the EHC. As a consequence, this seemingly small difference leads to significantly lower optimal temperatures for the EHC than for the WE, as discussed below in the context of the optimal system design.

Varying the current density and the membrane thickness shows similar qualitative effects on the WE and EHC energy demand. At reference conditions, however, both ohmic overpotentials have a relatively high impact on the EHC energy demand, whereas the gas-crossover losses are comparatively small. Therefore, at reference conditions, the optimal current density and membrane thickness of the EHC (Figs. 3b and 3d) are smaller compared to those of the WE (Figs. 2b and 2d).

Summarizing the parameter studies, the WE and EHC show similar characteristics concerning the isothermal compression behavior, the activation overpotential associated with the HER and the ohmic overpotentials if the same materials and loss mechanisms are considered for both devices. Large differences between the WE and the EHC characteristics, on the other hand, can be observed concerning the gas-crossover losses, the temperature dependence and the proportions of the individual overpotentials on the total energy demand.

Energetic evaluation and comparison of hydrogen production pathways.—So far, the WE and the EHC were examined in separate parameter studies to emphasize their general functionality. In the following, the focus is on the two hydrogen production pathways sketched in Fig. 1a. As a brief reminder, in PW I, hydrogen is generated via WE and subsequently compressed to delivery pressure via EHC. As a first variant of this pathway, the WE cathode pressure p^c_{WE} is fixed to ambient pressure. Consequently, the compression work is done solely by the EHC. In PW II, hydrogen generation and simultaneous co-compression to delivery pressure are provided solely by the WE. To point out generic differences between the pathways, the same design parameters are used for both devices that were already considered as reference conditions in the previous parameter studies, i.e. same current density ($i = 1$ A cm^{-2}), temperature ($T = 60$ °C) and membrane thickness ($\delta_m = 150$ μm).

The electrical energy demand for producing one kilogram of hydrogen at delivery pressures up to 1000 bar is shown in Fig. 4a for PW I and Fig. 4b for PW II. Analogously to the parameter studies, the total energy demand is divided into the energy demand without considering gas-crossover (non-hatched area) and the gas-crossover losses (hatched area). The pastel colored area in Fig. 4a represents the constant energy demand of the WE operating at ambient pressure

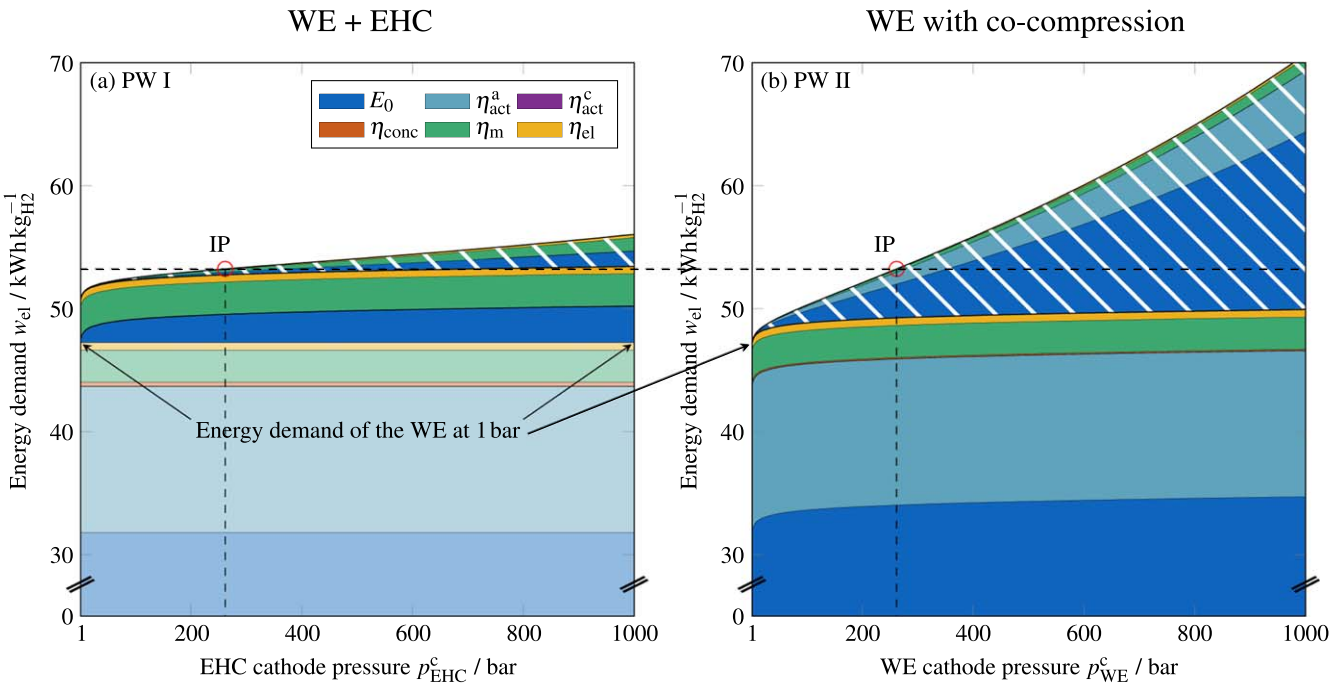

Figure 4. Energy demand of hydrogen production via (a) PW I: a WE operated at 1 bar (pastel colors) and a downstream EHC operated at delivery pressure (intense colors), and (b) PW II: a WE with co-compression operated at delivery pressure. The remaining parameters are at reference conditions for both systems ($i = 1$ A cm^{-2}, $T = 60$ °C, $\delta_m = 150$ μm). The red cycle marks the intersection point (IP) of the two curves, located at approximately 260 bar and 53 kWh kg$^{-1}_{H2}$.

(hydrogen generation), and the remaining area (intense colors) represents the energy demand of the downstream EHC (hydrogen compression).

As expected, the energy demand of both pathways increases with increasing delivery pressure due to an increasing thermodynamic cell voltage and increasing gas-crossover losses of the EHC in PW I and of the WE in PW II. Comparing both pathways reveals that the total energy demand of PW I is higher at pressure levels close to ambient pressure due to the additional EHC losses, such as proton transport losses through a second membrane. However, the energy demand of PW II shows a steeper slope with increasing delivery pressure. As already mentioned, the WE with co-compression suffers from significantly higher gas-crossover losses than the EHC due to the additional water splitting and OER kinetic losses. Consequently, low delivery pressures favor the WE with co-compression, whereas, considering the selected operating conditions, compression via EHC is less energy-intensive at pressures above approximately 260 bar, with the benefit strongly increasing towards higher pressures.

The comparison so far is of a rather theoretical nature. In reality, however, the delivery pressure is typically dependent on the application. The other parameters such as the current density, temperature and membrane thickness of both devices, on the other hand, can be adjusted within a certain range. In addition, the WE cathode pressure in PW I, which corresponds to the EHC anode pressure, is also adjustable. In the following, the pathways are optimized regarding the adjustable parameters to determine the minimum energy demand and to further analyze the advantages and disadvantages of both pathways.

Energetic optimization of hydrogen production pathways.— Two important hydrogen delivery pressure levels are chosen to exemplarily determine the optimal system configuration of the two pathways of interest. The energy demands of the pathways are then compared as a function of the delivery pressure and the current density. First, hydrogen production at 200 bar is investigated because this pressure level is common for storage, transportation and in many industrial applications like ammonia production.[21] Secondly, a hydrogen delivery pressure of 800 bar is chosen to meet the hydrogen refueling requirements associated with automotive applications, e.g. fuel cell electric vehicles.[22]

The current density range of interest is chosen between 0.5 A cm^{-2} and 5 A cm^{-2} in the following optimization for capital cost and efficiency reasons, respectively.[20,23] The temperature range is chosen between 20 °C and 80 °C for practical and lifetime issues, respectively.[24,25] The membrane thicknesses of the WE and the EHC are optimized without any limitations. Other parameters, such as catalyst materials or membrane types, obviously open up different optimization matrices, with the latter being discussed later.

If the aforementioned parameters are optimized with respect to the chosen parameter ranges, a minimum energy demand for a delivery pressure of 200 bar of 46.3 kWh kg$^{-1}_{H2}$ for PW I and 50.4 kWh kg$^{-1}_{H2}$ for PW II can be achieved, as summarized in Table II. Hence, hydrogen compression via EHC is approximately 4 kWh kg$^{-1}_{H2}$ more efficient than compression via WE. Furthermore, and in comparison with Fig. 4,

Table II. Minimum energy demand w^{min}_{el} and associated system configurations of hydrogen production via PW I and PW II at 200 bar delivery pressure. The listed parameters are optimized with regard to the given ranges.

Parameter	Range	PW I	PW II	Unit
p^{c}_{WE}	1–200	1	200[a)]	bar
i_{WE}	0.5–5	0.5	0.5	A cm^{-2}
T_{WE}	20–80	80	80	°C
$\delta_{m,WE}$	—	35	422	μm
p^{c}_{EHC}	—	200[a)]	—	bar
i_{EHC}	0.5–5	0.5	—	A cm^{-2}
T_{EHC}	20–80	20	—	°C
$\delta_{m,EHC}$	—	45	—	μm
w^{min}_{el}	—	46.3	50.4	kWh kg$^{-1}_{H2}$

a) Fixed as delivery pressure.

which shows the results for the reference conditions, the energy demand is reduced by 7 kWh kg_{H2}^{-1} for PW I and 2 kWh kg_{H2}^{-1} for PW II. Thus, at optimized conditions the pressure intersection point, from which compression via EHC is less energy-intensive than via WE, shifts from 260 bar at reference conditions all the way down to 4 bar.

Considering the energetically optimized system configurations, the WE cathode pressure in PW I is still at 1 bar, i.e. the compression work is done solely by the EHC. The optimal WE temperature in both PW I and PW II is 80 °C due to the significantly improved water splitting reaction and OER kinetics at elevated temperatures. The optimal EHC temperature, on the contrary, is at the lower limit of 20 °C to improve the compression efficiency since, unlike the WE, no water splitting reaction or OER occurs in the EHC. In absolute and relative terms, the proton transport losses through the membrane have a large influence on the EHC energy demand at low temperatures, which must be compensated for by means of relatively thin membranes. Moreover, the comparatively low gas-crossover losses in the EHC allow for significantly thinner membranes than for the WE in PW II. Therefore, the optimal EHC membrane is only 45 μm thick and one order of magnitude thinner than the optimal WE membrane at approximately the same pressure gradient. Even the sum of both membrane thicknesses of the WE and EHC membranes in PW I are still 342 μm thinner than the optimal membrane thickness of the high pressure WE in PW II. Summarizing, the separation of hydrogen generation and compression in PW I leads to (i) smaller absolute gas-crossover losses, (ii) thinner optimal membranes and reduced ohmic proton transport losses, and (iii) an improved compression efficiency due to a lower optimal compression temperature.

Regarding the current densities, the optimization reveals that both devices are most efficient at the lower parameter limit of 0.5 A cm^{-2}. In contrast, higher current densities are typically preferred from an economic perspective. Moreover, when connected to intermittent renewable energy sources, such as a wind or solar power plant, the WE and the EHC have to provide a relatively high operation flexibility, e.g. due to a high current density range, and thus high turndown ratio.

Therefore, the optimum configuration and the associated energy demand is shown as a function of the current densities between 0.5 A cm^{-2} and 5 A cm^{-2} in Fig. 5a for PW I and Fig. 5b for PW II. To allow for comparison to the energy demand required for hydrogen production at 800 bar which is discussed below, the colorbar in Fig. 5 depicts a wider range of energy demand than actually required for hydrogen production at 200 bar. An illustration with the colorbar representing only the energy demand at 200 bar is given in the supplementary material (available online at stacks.iop.org/JES/168/014504/mmedia).

In Fig. 5a, the color coding represents the minimum possible energy demand for every combination of WE current density (*y*-axis) and EHC current density (*x*-axis). In order to have similar hydrogen outputs for the WE and the EHC, the area and the number of cells of the devices must therefore differ but are not considered further. The contour lines show the corresponding optimized parameter values for the WE cathode pressure p_{WE}^{c}, WE membrane thickness $\delta_{m,WE}$ and EHC membrane thickness $\delta_{m,EHC}$. The optimal WE and EHC temperatures are constant at the maximum of 80 °C and the minimum of 20 °C throughout the investigated range of current densities, respectively, and therefore not illustrated with contour lines.

As previously mentioned, the global optimum with an energy demand of 46.3 kWh kg_{H2}^{-1} is at $i_{WE} = i_{EHC} = 0.5$ A cm^{-2}. From this point, every increase of the WE or EHC current density causes a higher energy demand up to a maximum of 56.4 kWh kg_{H2}^{-1} at $i_{WE} = i_{EHC} = 5$ A cm^{-2}. The optimal membrane thickness of both devices decreases with increasing current density for two reasons. First, more hydrogen is produced or compressed in total, and thus the relative impact of gas-crossover on the energy demand decreases. Second, higher current densities lead to higher ohmic losses, which are compensated for by decreasing the membrane thickness. This also explains the slight increase in WE cathode pressure, up to 3 bar, with

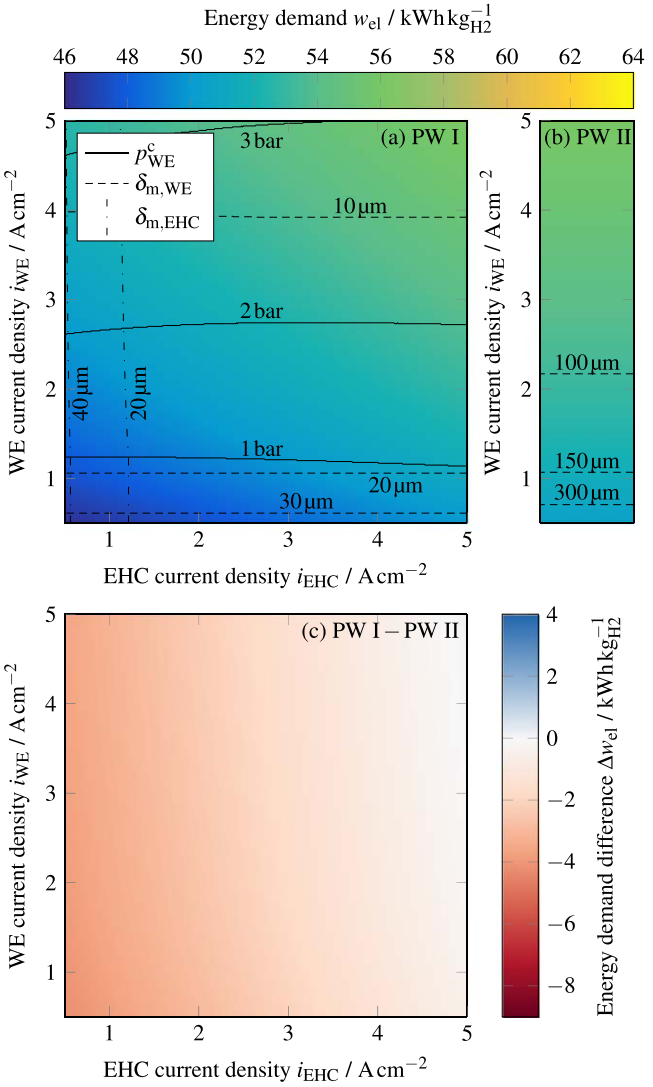

Figure 5. Energetically optimal hydrogen production at 200 bar using (a) PW I: a WE (with co-compression) and a downstream EHC, and (b) PW II: a WE with co-compression to delivery pressure. The contour lines represent the optimal parameter configurations as a function of the current densities. The optimal temperatures are at the chosen maximum parameter limit of $T_{WE} = 80$ °C for the WE and minimum parameter limit of $T_{EHC} = 20$ °C for the EHC throughout the considered current density ranges. (c) Additional energy demand of PW I compared to PW II at the same WE current density.

increasing current density, which is still relatively low compared to state of the art WEs that typically operate at pressures above 30 bar to reduce the downstream compression and drying effort.[5] If an EHC is also available, however, most of the compression work should be done by the EHC due to its relatively low gas-crossover losses.

Figure 5b shows the minimum energy demand of PW II, hydrogen production at 200 bar solely via WE, in dependence of the current density. The energy demand increases with increasing current density from the minimum of 50.4 kWh kg_{H2}^{-1} at 0.5 A cm^{-2} up to 56.2 kWh kg_{H2}^{-1} at 5 A cm^{-2}. Similar to PW I, the optimal membrane thickness of the WE decreases with increasing current density. Moreover, the optimal WE temperature is constant at the higher limit of 80 °C to favor the water splitting reaction and OER kinetics.

The energy demand difference Δw_{el} illustrated in Fig. 5c is calculated by subtracting the energy demand of PW II from the energy demand of PW I at the same WE current density, i.e. at approximately the same hydrogen production ratios in PW I and PW II considering similar WE active cell areas. Hence, a negative energy

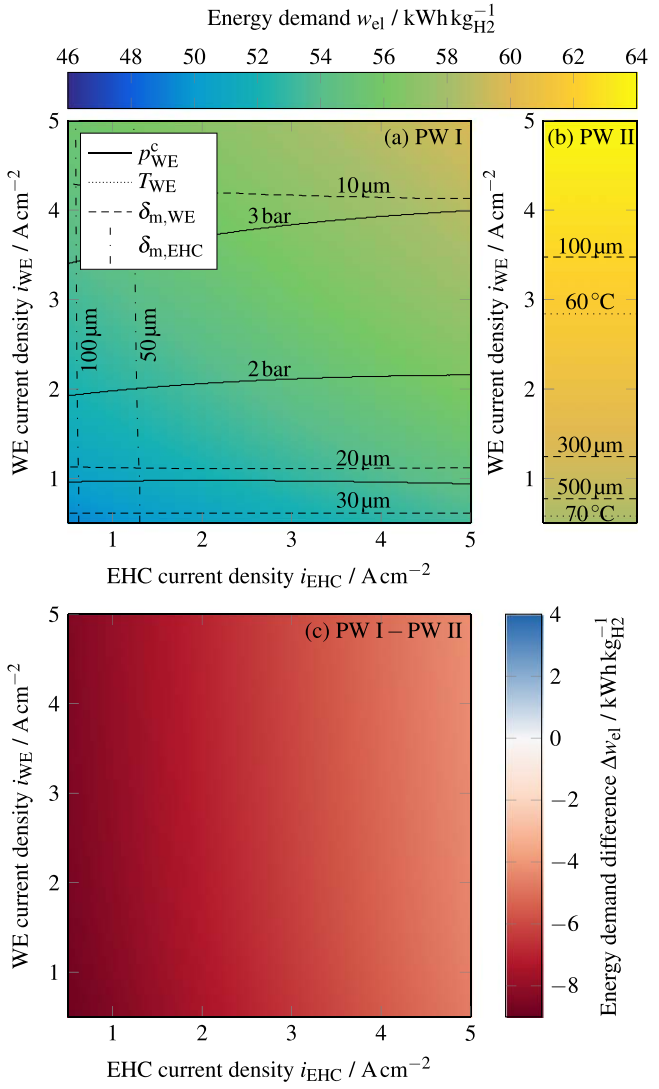

Figure 6. Energetically optimal hydrogen production at 800 bar using (a) PW I: a WE (with co-compression) and a downstream EHC, and (b) PW II: a WE with co-compression to delivery pressure. The contour lines represent the optimal parameter configurations as a function of the current densities. The optimal temperatures in (a) are at the chosen maximum parameter limit of $T_{WE} = 80$ °C for the WE and minimum parameter limit of $T_{EHC} = 20$ °C for the EHC throughout the considered current density ranges. (c) Additional energy demand of PW I compared to PW II at the same WE current density.

demand difference (red area) means that PW I is favorable, whereas a positive energy demand difference (blue area) means that PW II is favorable at that operating point. At the lower current density limit of 0.5 A cm^{-2}, PW I is almost 4 kWh kg$_{H2}^{-1}$, i.e. 8 % of the total energy demand, more efficient. At the higher current density limit of 5 A cm^{-2}, however, both pathways require roughly the same energy. It should be noted that the energy demand difference is almost independent of the WE current density if the WE current densities in PW I and PW II are varied equally (going along the *y*-axis in Fig. 5c).

Analogously to before, Figs. 6a and 6b present the optimal configurations of PW I and PW II for 800 bar hydrogen delivery pressure. In general, the qualitative results are similar to hydrogen production at 200 bar in Figs. 5a and 5b. However, the optimal WE temperature in PW II now differs from 80 °C, and obviously thicker membranes are needed for the EHC and the high pressure WE because hydrogen diffusion through the membrane is crucial at 800 bar delivery pressure. The energy demand difference in Fig. 6c is even more in favor of PW I due to the superior compression

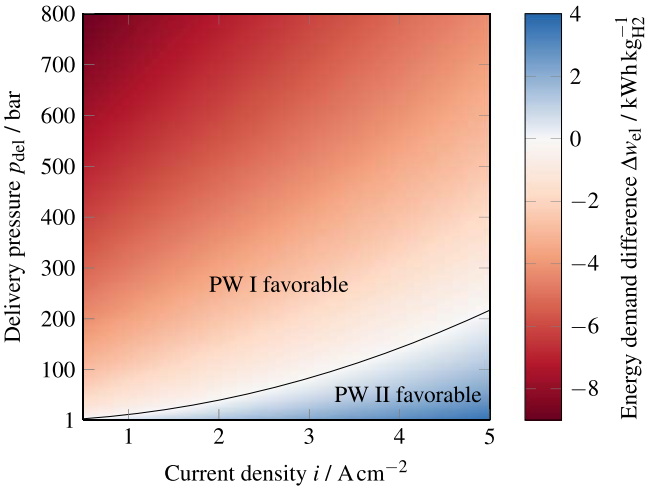

Figure 7. Additional energy demand of PW I compared to PW II as a function of the delivery pressure and the current density, which is varied equally for the WEs in PW I and PW II and the EHC in PW I. For every operating point, the energy demand difference is calculated based on optimized WE and EHC membrane thicknesses, optimized temperatures in the range between 20 °C and 80 °C and an optimized WE cathode pressure in PW I. The line indicates operating points with an equal energy demand of PW I and PW II.

efficiency of the EHC. Depending on the current density, PW I is approximately 4–8 kWh kg$_{H2}^{-1}$, i.e. 6–16 % of the total energy demand, less energy-intensive than PW II. Similar to before, the energy demand difference is approximately independent of the WE current density, if the WE current densities in PW I and PW II are varied equally. Therefore, in the following, the current densities of the WE and EHC are not considered separately any longer and are varied equally as well, which corresponds to going diagonal in Fig. 6c.

The comparison so far showed that, with regard to the chosen materials and parameter limits, an EHC should be favored for hydrogen compression over a high pressure WE at both investigated pressure levels, 200 bar and 800 bar. The achievable savings, however, depend strongly on the delivery pressure and the current density. Therefore, the energy demand difference Δw_{el} is calculated and presented in Fig. 7 as a function of both parameters, considering similar current densities for the WEs in PW I and PW II and the EHC in PW I. For every operating point in Fig. 7, the energy demand difference is again determined based on optimized WE and EHC membrane thicknesses, optimized temperatures in the range between 20 °C and 80 °C and an optimized WE cathode pressure in PW I.

The pressure intersection point above which PW I is favorable, increases with increasing current density from 4 bar at 0.5 A cm^{-2} up to 210 bar at 5 A cm^{-2}. The energy demand difference ranges from approximately −8 kWh kg$_{H2}^{-1}$ at 800 bar and 0.5 A cm^{-2} to 3 kWh kg$_{H2}^{-1}$ at 1 bar and 5 A cm^{-2}. Consequently, high delivery pressures clearly benefit the usage of an EHC for hydrogen compression. Moreover, if an EHC is used for downstream hydrogen compression, it should operate at the lowest possible current density to be most efficient. For a comprehensive evaluation, the investment cost would also have to be taken into account, which unfortunately goes beyond the scope of this work. Instead, the presented results provide a reference on how to minimize the energy demand, and thus the operating cost, of pressurized hydrogen supply while using electrochemical hydrogen generation and compression.

Discussion

In the previous section, the two hydrogen production pathways of interest were optimized for specific materials and parameter limitations. In order to meet different system requirements and adjust to

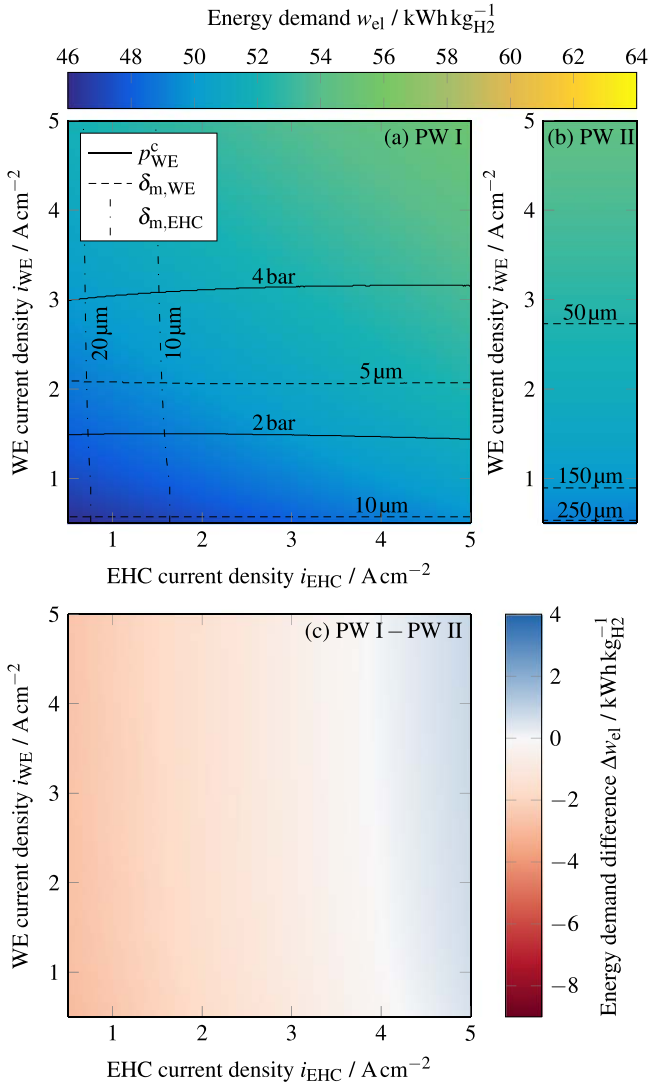

Figure 8. Energetically optimal hydrogen production at 800 bar using (a) PW I: a WE (with co-compression) and a downstream EHC, and (b) PW II: a WE with co-compression to delivery pressure. The contour lines represent the optimal parameter configurations as a function of the current densities. The optimal temperatures are at the chosen maximum parameter limit of $T_{WE} = 80$ °C for the WE and minimum parameter limit of $T_{EHC} = 20$ °C for the EHC throughout the considered current density ranges. (c) Additional energy demand of PW I compared to PW II at the same WE current density. Compared to Fig. 6, the gas-permeability of the WE and EHC membranes is set to 1/10 of the therein considered Nafion-based membranes.

new developments, the optimization can be done for other input parameters, such as different materials (e.g. PTFE reinforced membranes) or parameter boundaries (e.g. temperatures above 80 °C). One decisive parameter in high pressure operation is the membrane gas permeability, for which novel membranes, e.g. based on hydrocarbons, already show significantly improved ion conductivity and simultaneously reduced gas permeability, but reduced lifetime compared to state-of-the-art Nafion-based membranes.[26] In order to demonstrate the impact of the membrane gas permeability, its value is reduced to only 1/10 of that of a Nafion membrane and considered in the 800 bar scenario, as shown in Fig. 8.

Compared to the energy demand considering Nafion membranes shown in Fig. 6, the absolute energy demand is significantly reduced by approximately 4 kWh kg$_{H2}^{-1}$ for PW I and 9 kWh kg$_{H2}^{-1}$ for PW II. Apart from the reduced gas-crossover losses, this is also a consequence of reduced membrane thicknesses, as this results in lower ohmic losses. Comparatively speaking, the reduced membrane gas permeability favors PW II, as high gas-crossover losses are considered the main drawback of the WE with co-compression. Therefore, at EHC current densities above 4 A cm^{-2}, PW II is even less energy-intensive than PW I.

Regarding the optimal system configurations, the WE cathode pressure in PW I is slightly higher in Fig. 8a, but still does not exceed a maximum of 6 bar. Similar to before, the optimal EHC temperature is at the minimum of 20 °C to allow for efficient compression. Consequently, improving the membrane conductivity, especially at low operating temperatures, would considerably improve the efficiency of high pressure EHC operation. As expected, the optimal membrane thickness of both the EHC and the high pressure WE decreases drastically due to the improved gas permeability of the membrane. It should be noted that the optimal EHC membrane thickness is now in the range of only 5–30 μm, even at a differential pressure of almost 800 bar. Moreover, the optimal WE membrane thickness is also in the range of only 5–10 μm in PW I and 70–270 μm in PW II, indicating the need to ensure sufficient (mechanical) stability of the membranes and safety standards. This development goal could be achieved by a better mechanical support of the membrane, e.g. in the form of a microporous layer,[27] or by adding a reinforced layer, e.g. based on PTFE, similar to developments in PEM fuel cells with membrane thicknesses smaller than 25 μm.[20,25]

Conclusions

The present study analysis the energy demand of pressurized hydrogen supply for delivery pressures up to 1000 bar using PEM water electrolyzers and PEM electrochemical hydrogen compressors. From a theoretical perspective, both WE and EHC follow an isothermal compression behavior. For real applications, however, the WE suffers from high gas-crossover losses due to the additional water splitting and OER kinetic losses, whereas the EHC simply re-compresses permeated hydrogen. Consequently, at the same hydrogen outlet pressure and operating conditions, the losses associated with gas-crossover are significantly higher for the WE than for the EHC, which, from an energetic perspective, is the main disadvantage of direct co-compression in the WE. However, this disadvantage decreases with increasing current density because the relative impact of gas-crossover on the total energy demand decreases. While using an EHC is already favorable to co-compression via WE above pressures of 4 bar at a current density of 0.5 A cm^{-2}, this pressure intersection point shifts up to 210 bar at 5 A cm^{-2}.

Hydrogen delivery pressures of 200 bar and 800 bar were chosen exemplarily to optimize the system configurations of the two hydrogen production pathways that consider both electrochemical hydrogen generation and compression: In PW I, hydrogen is generated (and co-compressed) via WE and subsequently compressed to delivery pressure via EHC, whereas in PW II, hydrogen is generated and compressed to delivery pressure solely via WE. Depending on the applied current densities, considered between 0.5 A cm^{-2} and 5 A cm^{-2}, PW I is up to 4 kWh kg$_{H2}^{-1}$, i.e. 8 % of the total energy demand, more energy efficient at 200 bar and 4–8 kWh kg$_{H2}^{-1}$, i.e. 6–16 %, at 800 bar.

The superior efficiency of PW I over PW II at elevated delivery pressures is attributed to the separation of hydrogen generation and compression. Thereby, (i) the losses associated with gas-crossover are reduced due to the re-compression of permeated hydrogen in the EHC, (ii) the ohmic proton transport losses are reduced because thinner membranes can be used, and (iii) the temperature can be optimized separately for both devices. While the WE is most efficient at temperatures above 80 °C due to improved water splitting and OER kinetics, the EHC energy demand is minimized at temperatures below 20 °C due to improved compression efficiency.

Finally, the development goals of membranes were demonstrated by means of improved gas permeability, which not only reduces the gas-crossover losses, but also allows for significantly thinner membranes. Hence, ensuring the mechanical stability of membranes

while maintaining the ion conductivity is found to be one of the major challenges for the application of efficient, high pressure electrochemical hydrogen compression.

This work provides guidance on how to minimize the energetic cost, and thereby the operating cost of pressurized hydrogen supply using WEs and EHCs. In follow-up work, the investment cost should also be considered to allow for a more comprehensive evaluation and optimization. Furthermore, comparing the investigated hydrogen production pathways to pathways considering state-of-the-art mechanical compressors, both energetically and economically, is of great interest for future system design.

Acknowledgments

We thank Sheridan Renzi for proofreading the manuscript. The publication of this article was funded by the Open Access Fund of Leibniz Universität Hannover.

Appendix: Model Description

The main model equations of the WE and EHC models are discussed in the theory section. Starting with the WE, the complementary model equations are given in the following. A complete list of the associated parameter values is given at the end of the appendixin Table A·I.

A.1. Water electrolyzer.—The thermodynamic cell voltage of the WE is determined by the Nernst equation:

$$E_0 = \frac{\Delta G}{2 \cdot \mathrm{F}} + \frac{\mathrm{R} \cdot T}{2 \cdot \mathrm{F}} \cdot \ln\left(\frac{a_{\mathrm{H2}} \cdot \sqrt{a_{\mathrm{O2}}}}{a_{\mathrm{H2O}}}\right) \quad [\mathrm{A}\cdot1]$$

where ΔG is the molar change in Gibbs free energy during the water splitting reaction that is obtained from the National Institut of Standards and Technology Chemistry WebBook,[28] R is the molar gas constant, F is the Faraday constant, T is the temperature and a is the activity. The activity of water is considered as one, whereas the activity of hydrogen and oxygen can be expressed as[40]

$$a_{\mathrm{i}} = \frac{f_{\mathrm{i}}}{p_{\mathrm{ref}}} = \frac{\varphi_{\mathrm{i}} \cdot p_{\mathrm{i}}}{p_{\mathrm{ref}}} = \frac{\exp(Z_{\mathrm{i}} - 1) \cdot p_{\mathrm{i}}}{p_{\mathrm{ref}}} \quad [\mathrm{A}\cdot2]$$

Herein, p_{ref} is the reference pressure that is defined as 1 bar in this work, f_{i} is the fugacity, ϕ_{i} is the fugacity coefficient, p_{i} is the partial pressure and Z_{i} is the compressibility factor of species i. The compressibility factor describes the deviation of a real gas from the ideal gas behavior and is defined as

$$Z_{\mathrm{i}} = \frac{p_{\mathrm{i}} \cdot V_{\mathrm{i}}}{n_{\mathrm{i}} \cdot \mathrm{R} \cdot T} \quad [\mathrm{A}\cdot3]$$

where V_{i} is the volume of the gas and n_{i} is the number of moles. Since the oxygen pressure is kept at ambient pressure in this work, it is assumed to behave as an ideal gas with $Z_{\mathrm{O2}} = 1$. For hydrogen, on the other hand, the deviation from an ideal gas has to be considered due to the high partial pressures investigated. The hydrogen compressibility factor is calculated based on a temperature and pressure dependent approximation of Zheng et al.[29] Combining Eqs. A·1–A·3, the thermodynamic cell voltage can be expressed as

$$E_0 = \frac{\Delta G}{2 \cdot \mathrm{F}} + \frac{\mathrm{R} \cdot T}{2 \cdot \mathrm{F}} \cdot \left(Z_{\mathrm{H2}}(p_{\mathrm{H2}}^{\mathrm{c,ch}}) - Z_{\mathrm{H2}}(p_{\mathrm{ref}}) + \ln\left(\frac{p_{\mathrm{H2}}^{\mathrm{c,ch}}}{p_{\mathrm{ref}}}\right) + \frac{1}{2} \cdot \ln\left(\frac{p_{\mathrm{O2}}^{\mathrm{a,ch}}}{p_{\mathrm{ref}}}\right)\right) \quad [\mathrm{A}\cdot4]$$

The product gases are assumed to be fully humidified at the cell outlets, and therefore the partial pressures of hydrogen in the cathodic channel and oxygen in the anodic channel can be determined by subtracting the saturated water vapor pressure from the absolute obtained pressure:

$$p_{\mathrm{H2}}^{\mathrm{c,ch}} = p^{\mathrm{c,ch}} - p_{\mathrm{H2O}}^{\mathrm{sat}} \quad [\mathrm{A}\cdot5]$$

$$p_{\mathrm{O2}}^{\mathrm{a,ch}} = p^{\mathrm{a,ch}} - p_{\mathrm{H2O}}^{\mathrm{sat}} \quad [\mathrm{A}\cdot6]$$

Here $p^{\mathrm{c,ch}}$ and $p^{\mathrm{a,ch}}$ are the default absolute pressures in the cathodic and anodic channel. The saturated water vapor pressure $p_{\mathrm{H2O}}^{\mathrm{sat}}$ is approximated with an equation from Wagner and Kretzschmar.[30]

The activation overpotentials of the WE are calculated via the Butler-Volmer equation[15]:

$$i = i_0 \cdot \left[\exp\left(\frac{\overleftarrow{\alpha} \cdot \mathrm{F} \cdot \eta_{\mathrm{act}}}{\mathrm{R} \cdot T}\right) - \exp\left(\frac{-\overrightarrow{\alpha} \cdot \mathrm{F} \cdot \eta_{\mathrm{act}}}{\mathrm{R} \cdot T}\right)\right] \quad [\mathrm{A}\cdot7]$$

In Eq. A·7, i_0 is the apparent exchange current density, $\overleftarrow{\alpha}$ is the anodic transfer coefficient and $\overrightarrow{\alpha}$ the cathodic transfer coefficient. For the OER on iridium oxide at the anode, the Butler-Volmer equation simplifies to the Tafel equation due to significant overpotentials even at relatively small current densities[15]:

$$\eta_{\mathrm{act}}^{\mathrm{a}} = \frac{\mathrm{R} \cdot T}{\overleftarrow{\alpha}^{\mathrm{a}} \cdot \mathrm{F}} \cdot \ln\left(\frac{i}{i_0^{\mathrm{a}}}\right) \quad [\mathrm{A}\cdot8]$$

The kinetic parameters depend strongly on the electrode and catalyst materials used. In this work, an anodic transfer coefficient $\overleftarrow{\alpha}^{\mathrm{a}}$ of 0.84 is chosen for the OER, which is based on measurements with an iridium oxide-based catalyst.[18] The temperature dependence of the apparent exchange current density is modeled using an Arrhenius approach[41,42]:

$$i_0^{\mathrm{a}} = i_{0,\mathrm{ref}}^{\mathrm{a}} \cdot \exp\left[-\frac{E_{\mathrm{A}}^{\mathrm{a}}}{\mathrm{R}} \cdot \left(\frac{1}{T} - \frac{1}{T_{\mathrm{ref}}^{\mathrm{a}}}\right)\right] \quad [\mathrm{A}\cdot9]$$

Herein, $E_{\mathrm{A}}^{\mathrm{a}}$ is the activation energy of the OER with 67 kJ mol^{-1} [31] and $i_{0,\mathrm{ref}}^{\mathrm{a}}$ is the corresponding apparent exchange current density on iridium oxide with approximately 1×10^{-6} A cm^{-2} at a reference temperature $T_{\mathrm{ref}}^{\mathrm{a}}$ of 323 K.[18]

The cathodic activation overpotential belongs to the quasi-reversible HER on platinum, and thus the Butler-Volmer equation can be linearized to[15,16]:

$$\eta_{\mathrm{act}}^{\mathrm{c}} = \frac{\mathrm{R} \cdot T}{\mathrm{F} \cdot (\overleftarrow{\alpha}^{\mathrm{c}} + \overrightarrow{\alpha}^{\mathrm{c}})} \cdot \frac{i}{i_0^{\mathrm{c}}} \quad [\mathrm{A}\cdot10]$$

The temperature dependence of the cathodic exchange current density is also described using an Arrhenius approach according to Eq. A·11.

$$i_0^{\mathrm{c}} = L_{\mathrm{Pt}} \cdot A_{\mathrm{Pt,el}} \cdot i_{0,\mathrm{s,ref}}^{\mathrm{c}} \cdot \exp\left[-\frac{E_{\mathrm{A}}^{\mathrm{c}}}{\mathrm{R}} \cdot \left(\frac{1}{T} - \frac{1}{T_{\mathrm{ref}}^{\mathrm{c}}}\right)\right] \quad [\mathrm{A}\cdot11]$$

Here, L_{Pt} is the cathode catalyst loading that is assumed to be 3.5 g_{Pt} m^{-2} in this work, $A_{\mathrm{Pt,el}}$ is the the electrochemically active surface area equal to 60 m^2 g_{Pt}^{-1} [33] and $i_{0,\mathrm{s,ref}}^{\mathrm{c}}$ is the catalyst-specific exchange current density referring to the active catalyst surface at reference temperature $T_{\mathrm{ref}}^{\mathrm{c}}$. The kinetic paramters of the HER were determined by Durst et al. at carbon supported platinum catalysts for different temperatures.[32] With the sum of the transfer coefficients fixed to one ($\overleftarrow{\alpha}^{\mathrm{c}} + \overrightarrow{\alpha}^{\mathrm{c}} = 1$), the specific exchange current density is approximately 135 mA $\mathrm{cm}_{\mathrm{Pt}}^{-2}$ at a reference temperature of 313 K and an activation energy $E_{\mathrm{A}}^{\mathrm{c}}$ of 16 kJ mol^{-1}. Considering the chosen

parameters, Eq. A·11 results in an apparent exchange current density of approximately 41 A cm^{-2} at 60 °C for the HER on platinum at the WE cathode.

Mass transport resistances between the catalyst layer and channel lead to an increased concentration of the product gases at the catalyst layer. The thereof resulting concentration overpotential η_{conc} is defined by Eq. A·12 as the sum of the anodic and cathodic concentration overpotential.

$$\eta_{conc} = \eta^{a}_{conc} + \eta^{c}_{conc} \quad [A\cdot12]$$

Similar to the Nernst equation, the voltage increase can be determined as

$$\eta^{a}_{conc} = \frac{R \cdot T}{4 \cdot F} \cdot \ln\left(\frac{p^{a,cl}_{O2}}{p^{a,ch}_{O2}}\right) \quad [A\cdot13]$$

for the anode and

$$\eta^{c}_{conc} = \frac{R \cdot T}{2 \cdot F} \cdot \left(Z_{H2}(p^{c,cl}_{H2}) - Z_{H2}(p^{c,ch}_{H2}) + \ln\left(\frac{p^{c,cl}_{H2}}{p^{c,ch}_{H2}}\right)\right) \quad [A\cdot14]$$

for the cathode. In Eqs. A·13 and A·14, the partial pressures are equivalent to the the dissolved gas concentrations at the catalyst layer and the channel according to Henry's law. For hydrogen, the deviation from an ideal gas is again considered by using the compressibility factor (see Eqs. A·1–A·4).

Based on Refs. 43 and 44, the partial pressures of the evolving product gases at the catalyst layer $p^{a,cl}_{O2}$ and $p^{c,cl}_{H2}$ are determined by the mass balances for oxygen at the anodic reaction zone (Eq. A·15) and hydrogen at the cathodic reation zone (Eq. A·16). The following equation system must be solved to obtain the partial pressures in dependence of the current density:

$$\text{Anode: } \underbrace{\frac{i}{4 \cdot F}}_{N^{evo}_{O2}} = \underbrace{k^{a}_{L,O2} \cdot S_{O2} \cdot (p^{a,cl}_{O2} - p^{a,ch}_{O2})}_{N^{a,out}_{O2}} + \underbrace{\frac{D^{eff}_{O2} \cdot S_{O2}}{\delta_m} \cdot (p^{a,cl}_{O2} - p^{c,cl}_{O2})}_{N^{perm}_{O2}} + \underbrace{\frac{1}{2} \cdot \frac{D^{eff}_{H2} \cdot S_{H2}}{\delta_m} \cdot (p^{c,cl}_{H2} - p^{a,cl}_{H2})}_{1/2 \cdot N^{perm}_{H2}} \quad [A\cdot15]$$

$$\text{Cathode: } \underbrace{\frac{i}{2 \cdot F}}_{N^{evo}_{H2}} = \underbrace{k^{c}_{L,H2} \cdot S_{H2} \cdot (p^{c,cl}_{H2} - p^{c,ch}_{H2})}_{N^{c,out}_{H2}} + \underbrace{\frac{D^{eff}_{H2} \cdot S_{H2}}{\delta_m} \cdot (p^{c,cl}_{H2} - p^{a,cl}_{H2})}_{N^{perm}_{H2}} + \underbrace{2 \cdot \frac{D^{eff}_{O2} \cdot S_{O2}}{\delta_m} \cdot (p^{a,cl}_{O2} - p^{c,cl}_{O2})}_{2 \cdot N^{perm}_{O2}} \quad [A\cdot16]$$

The left-hand side of Eqs. A·15 and A·16 represents the total amount of produced product gas at the respective catalyst layer according to Faraday's law.

The first term on the right-hand side describes the mass transfer from the catalyst layer to the channel with S_i as the solubility of the respective gas in water and $k_{L,i}$ as the mass transfer coefficient. The solubilities of the product gases in dependence of the temperature are obtained from Battino et al. for oxygen[35] and from Young et al. for hydrogen.[37] The mass transfer coefficient combines all mass transport resistances like desorption and diffusion and depends on the catalyst and electrode materials used. For hydrogen, a mass transfer coefficient $k^{c}_{L,H2}$ of 110×10^{-3} m s^{-1} was determined via gas-crossover measurements at Pt/C catalysts and a Nafion-based membrane.[34] The mass transfer coefficient of oxygen $k^{a}_{L,O2}$ is assumed to be approximately half of the hydrogen mass transfer coefficient due to its bigger molecular size, which is in good accordance with the ratio of the oxygen and hydrogen diffusion coefficients.

The second term on the right-hand side describes the permeation of the dissolved gases through the membrane according to Fick's law of diffusion with D^{eff}_{i} as the effective diffusion coefficient of the dissolved gas in the membrane and δ_m as the membrane thickness. Typically the Bruggemann's correlation is used to determine the effective diffusion coefficient[45,46]:

$$D^{eff}_{i} = D_i \cdot \frac{\epsilon_m}{\tau_m} \quad [A\cdot17]$$

Herein, the diffusion coefficient of the dissolved gas in water D_i is corrected by the membrane's porosity ϵ_m and its geometric tortuosity τ_m. The temperature dependent diffusion coefficients of oxygen and hydrogen in water are obtained from Wise and Houghton and are approximately $D^{eff}_{O2} = 5.5 \times 10^{-9}$ m^2 s^{-1} and $D^{eff}_{H2} = 12.4 \times 10^{-9}$ m^2 s^{-1} at 60 °C.[36] Furthermore, a porosity of $\epsilon_m = 0.37$ and a geometric tortuosity of $\tau_m = 1.5$ are assumed in this work.[38] The partial pressures of oxygen at the cathode $p^{c,cl}_{O2}$ and hydrogen at the anode $p^{a,cl}_{H2}$ in Eqs. A·15 and A·16 are negligibly small. At the cathode platinum particles, oxygen and hydrogen naturally react back to water, and at the anode, the application of a recombining catalyst is assumed to assure safe operation.[47] Moreover, the anode is operated at ambient pressure, and therefore the anodic partial pressure of hydrogen is always small compared to the cathodic hydrogen partial pressure and does not significantly affect the concentration gradient.

The third term on the right-hand side of Eqs. A·15 and A·16 describes the loss of evolving product gas due to the aforementioned reaction with permeated product gas from the opposing electrode, i.e. oxygen gas-crossover causes hydrogen losses at the cathodic reaction zone at a stoichiometric ratio of 1:2, and vice versa. Finally, both equations can be solved together to determine the partial pressures of the evolving product gases at the respective catalyst layer.

The ionic ohmic overpotential due to proton transport resistance of the membrane is calculated according to Ohm's law:

$$\eta_m = \frac{i \cdot \delta_m}{\sigma_m} \text{ with } \sigma_m = 100 \cdot (0.005139 \cdot \lambda_m - 0.003260) \cdot \exp\left[1268 \cdot \left(\frac{1}{303} - \frac{1}{T}\right)\right] \quad [A\cdot18]$$

Here, the proton conductivity σ_m is obtained from Springer et al. for a Nafion membrane.[17] Furthermore, the membrane is assumed to be fully hydrated with a water content of $\lambda_m = 21$ H_2O $(SO_3H)^{-1}$.[48]

The electrical ohmic overpotential due to bulk and interfacial resistance between the electrodes is determined by

$$\eta_{el} = i \cdot R_{el} \quad [A\cdot19]$$

where R_{el} is the electrical area resistance of the cell that is approximately independent of the temperature in the investigated range between 20 °C and 80 °C. Therefore, a constant value of $R_{el} = 23$ mΩ cm^2 is assumed.[18]

A.2. EHC.—If not stated differently, the material parameters used in the EHC model are similar to the aforementioned parameters in the WE model. With regard to Eqs. A·1–A·3, the thermodynamic cell voltage of the EHC is defined as

$$E_0 = \frac{\mathrm{R}\cdot T}{2\cdot \mathrm{F}}\cdot\left(Z_{\mathrm{H2}}(p_{\mathrm{H2}}^{\mathrm{c,ch}}) - Z_{\mathrm{H2}}(p_{\mathrm{H2}}^{\mathrm{a,ch}}) + \ln\left(\frac{p_{\mathrm{H2}}^{\mathrm{c,ch}}}{p_{\mathrm{H2}}^{\mathrm{a,ch}}}\right)\right) \quad [\mathrm{A}\cdot 20]$$

Hydrogen is assumed to be fully humidified in the anodic and cathodic channel, and thus the partial pressures are determined by subtracting the saturated water vapor pressure from the absolute default pressure in the respective channel (see Eqs. A·5 and A·6).

The cathodic activation overpotential of the HER is calculated similar to the WE cathodic activation overpotential (Eq. A·8). Furthermore, the kinetic parameters of the HOR at the EHC anode are considered similar to the HER kinetic parameters,[32] and thus both the anodic and the cathodic activation overpotential are determined by

$$\eta_{\mathrm{act}}^{\mathrm{a}} = \eta_{\mathrm{act}}^{\mathrm{c}} = \frac{\mathrm{R}\cdot T}{\mathrm{F}\cdot(\overleftarrow{\alpha}^{\mathrm{c}} + \overrightarrow{\alpha}^{\mathrm{c}})}\cdot\frac{i}{i_0^{\mathrm{c}}} \quad [\mathrm{A}\cdot 21]$$

Unlike the WE, hydrogen is electrochemically consumed at the EHC anode, causing a concentration decrease from the anodic channel to the catalyst layer. The associated concentration overpotential is determined by Eq. A·22.

$$\eta_{\mathrm{conc}}^{\mathrm{a}} = \frac{\mathrm{R}\cdot T}{2\cdot \mathrm{F}}\cdot\left(Z_{\mathrm{H2}}(p_{\mathrm{H2}}^{\mathrm{a,ch}}) - Z_{\mathrm{H2}}(p_{\mathrm{H2}}^{\mathrm{a,cl}}) + \ln\left(\frac{p_{\mathrm{H2}}^{\mathrm{a,ch}}}{p_{\mathrm{H2}}^{\mathrm{a,cl}}}\right)\right) \quad [\mathrm{A}\cdot 22]$$

The cathodic concentration overpotential, on the other hand, is calculated similar to the WE cathodic concentration overpotential (Eq. A·14).

The partial pressures of hydrogen at the anodic and cathodic catalyst layer are determined by the following equation system, representing the mass balances at the respective reaction zone:

$$\text{Anode:}\quad \underbrace{\frac{i}{2\cdot\mathrm{F}}}_{N_{\mathrm{H2}}^{\mathrm{oxi}}} = \underbrace{k_{\mathrm{L,H2}}^{\mathrm{a}}\cdot S_{\mathrm{H2}}\cdot(p_{\mathrm{H2}}^{\mathrm{a,ch}} - p_{\mathrm{H2}}^{\mathrm{a,cl}})}_{N_{\mathrm{H2}}^{\mathrm{a,in}}} + \underbrace{\frac{D_{\mathrm{H2}}^{\mathrm{eff}}\cdot S_{\mathrm{H2}}}{\delta_{\mathrm{m}}}\cdot(p_{\mathrm{H2}}^{\mathrm{c,cl}} - p_{\mathrm{H2}}^{\mathrm{a,cl}})}_{N_{\mathrm{H2}}^{\mathrm{perm}}} \quad [\mathrm{A}\cdot 23]$$

$$\text{Cathode:}\quad \underbrace{\frac{i}{2\cdot\mathrm{F}}}_{N_{\mathrm{H2}}^{\mathrm{evo}}} = \underbrace{k_{\mathrm{L,H2}}^{\mathrm{c}}\cdot S_{\mathrm{H2}}\cdot(p_{\mathrm{H2}}^{\mathrm{c,cl}} - p_{\mathrm{H2}}^{\mathrm{c,ch}})}_{N_{\mathrm{H2}}^{\mathrm{c,out}}} + \underbrace{\frac{D_{\mathrm{H2}}^{\mathrm{eff}}\cdot S_{\mathrm{H2}}}{\delta_{\mathrm{m}}}\cdot(p_{\mathrm{H2}}^{\mathrm{c,cl}} - p_{\mathrm{H2}}^{\mathrm{a,cl}})}_{N_{\mathrm{H2}}^{\mathrm{perm}}} \quad [\mathrm{A}\cdot 24]$$

The left-hand side of Eqs. A·23 and A·24 describes the amount of hydrogen that is electrochemically consumed at the anode and electrochemically produced at the cathodic catalyst layer. The first term on the right-hand side is the hydrogen flux from the anodic channel to the catalyst layer in Eq. A·23 and the hydrogen transport from the cathodic catalyst layer to the channel in Eq. A·24. The second term on the right-hand side in both equations describes the gas-crossover from the cathode to the anode through the membrane.

The mass transfer coefficient of hydrogen from the cathodic catalyst layer to the cathodic channel $k_{\mathrm{L,H2}}^{\mathrm{c}}$ is assumed to be similar to the WE. At the anode, however, different processes like adsorption rather than desorption occur, and hence the mass transfer coefficient may also differ. In their work, Spingler et al. determined a mass transfer coefficient for gaseous hydrogen of approximately $k_{\mathrm{L,H2}}^{\mathrm{a,gas}} = 50\ \mathrm{mm\ s^{-1}}$ at a reference temperature of $T_{\mathrm{kL,ref}}^{\mathrm{a}} = 293.15\ \mathrm{K}$.[39] In Eq. A·23, however, hydrogen mass transfer and the corresponding mass transfer coefficient are considered for the dissolved phase, rather than the gaseous phase. Therefore, the mass transfer coefficient obtained by Spingler et al. has to be corrected to fit this model via

$$k_{\mathrm{L,H2}}^{\mathrm{a}} = k_{\mathrm{L,H2}}^{\mathrm{a,gas}}\cdot\frac{1}{S_{\mathrm{H2}}(293.15\ \mathrm{K})\cdot\mathrm{R}\cdot T_{\mathrm{kL,ref}}^{\mathrm{a}}} \quad [\mathrm{A}\cdot 25]$$

The correction factor $S_{\mathrm{H2}}\cdot\mathrm{R}\cdot T$ in Eq. A·25 corresponds to the conversion factor of a gaseous hydrogen concentration into a dissolved concentration according to the ideal gas law (Eq. A·26) and Henry's law (Eq. A·27).

$$p_{\mathrm{H2}} = c_{\mathrm{H2}}^{\mathrm{gas}}\cdot\mathrm{R}\cdot T \quad [\mathrm{A}\cdot 26]$$

$$p_{\mathrm{H2}} = \frac{c_{\mathrm{H2}}^{\mathrm{dis}}}{S_{\mathrm{H2}}} \quad [\mathrm{A}\cdot 27]$$

The mass transport coefficients are considered independent of the temperature and pressure in this work because a proper model-theoretical description is still missing. The impact on the results, however, is negligibly small.

Table A·I. Parameter values used in this work and the associated references. A value of f(T, p) indicates that the parameter is calculated in dependence of temperature and pressure and not defined by an equation above. In that case, reference to the original equation is given. Pressure, current density, temperature and membrane thickness are varied in this work, and thus not listed in the table.

Parameter	Value	Unit	Source
M_{H2}	2.0159	g mol^{-1}	28
ΔG	f(T)	J mol^{-1}	28
R	8.314	J mol^{-1} K^{-1}	—
F	96485.33	A s mol^{-1}	—
Z_{H2}	f(T, p)	—	29
Z_{O2}	1	—	—
p_{ref}	101325	Pa	—
$p_{\mathrm{H2O}}^{\mathrm{sat}}$	f(T, p)	Pa	30
$\overleftarrow{\alpha}^{\mathrm{a}}$	0.84	—	18
$i_{0,\mathrm{ref}}^{\mathrm{a}}$	1×10^{-6}	A cm^{-2}	18
$E_{\mathrm{A}}^{\mathrm{a}}$	67	kJ mol^{-1}	31
$T_{\mathrm{ref}}^{\mathrm{a}}$	323	K	18
$\overleftarrow{\alpha}^{\mathrm{c}} + \overrightarrow{\alpha}^{\mathrm{c}}$	1	—	32
$i_{0,\mathrm{s,ref}}^{\mathrm{c}}$	135	mA cm$_{\mathrm{Pt}}^{-2}$	32
L_{Pt}	3,5	g$_{\mathrm{Pt}}$ m^{-2}	33
$A_{\mathrm{Pt,el}}$	60	m^2 g$_{\mathrm{Pt}}^{-1}$	33
$E_{\mathrm{A}}^{\mathrm{c}}$	16	kJ mol^{-1}	32
$T_{\mathrm{ref}}^{\mathrm{c}}$	313	K	32
$k_{\mathrm{L,O2}}^{\mathrm{a}}$	55×10^{-3}	m s^{-1}	—
$k_{\mathrm{L,H2}}^{\mathrm{c}}$	110×10^{-3}	m s^{-1}	34
S_{O2}	f(T)	mol m^{-3} Pa^{-1}	35
D_{O2}	f(T)	m^2 s^{-1}	36
S_{H2}	f(T)	mol m^{-3} Pa^{-1}	37
D_{H2}	f(T)	m^2 s^{-1}	36
ϵ_{m}	0.37	—	38
τ_{m}	1.5	—	38
λ_{m}	21	H$_2$O (SO$_3$H)$^{-1}$	17
R_{el}	23	mΩ cm^2	18
$k_{\mathrm{L,H2}}^{\mathrm{a,gas}}$	50	mm s^{-1}	39
$T_{\mathrm{kL,ref}}^{\mathrm{a}}$	293.15	K	39

Finally, the ionic and electrical ohmic overpotentials are calculated similarly to the WE (Eqs. A·18 and A·19).

ORCID

Lars Zachert https://orcid.org/0000-0002-9137-7596
Michel Suermann https://orcid.org/0000-0001-9685-7081
Boris Bensmann https://orcid.org/0000-0001-8685-7192
Richard Hanke-Rauschenbach https://orcid.org/0000-0002-1958-307X

References

1. eurostat, (2020), Renewable Energy Statistics [Online]. Available: https://ec.europa.eu/eurostat/statistics-explained/index.php?title=Renewable_energy_statistics#Wind_power_is_the_most_important_renewable_source_of_electricity.
2. C. J. Barnhart, M. Dale, A. R. Brandt, and S. M. Benson, "The energetic implications of curtailing versus storing solar- and wind-generated electricity." *Energy & Environmental Science*, **6**, 2804 (2013).
3. T. Smolinka, E. T. Ojong, and J. Garche, "Hydrogen production from renewable energies–electrolyzer technologies." *Electrochemical Energy Storage for Renewable Sources and Grid Balancing* (Elsevier, Amsterdam) p. 103 (2015).
4. J. Eichmann, K. Harrison, and M. Peters, "Novel electrolyzer applications: providing more than just hydrogen." *National Renewable Energy Laboratory, Ed., Springfield* (2014), [Online]. Available: https://www.nrel.gov/docs/fy14osti/61758.pdf.
5. B. Bensmann, R. Hanke-Rauschenbach, G. Müller-Syring, M. Henel, and K. Sundmacher, "Optimal configuration and pressure levels of electrolyzer plants in context of power-to-gas applications." *Applied Energy*, **167**, 107 (2016).
6. M. Stefan, "From prototype to serial production—manufacturing hydrogen fuelling stations." *20th World Hydrogen Energy Conference 2014, Ed.* (2014).
7. H. Ishikawa, E. Haryu, N. Kawasaki, and H. Daimon, "Development of 70 mpa differential-pressure water electrolysis stack." *Honda R&D Technical Review*, **28**, 86 (2016).
8. P. J. Bouwman, J. Konink, D. Semerel, L. Raymakers, M. Koeman, W. Kout, W. Dalhuijsen, E. Milacic, and M. J. J. Mulder, "Electrochemical hydrogen compression." *ECS Trans.*, **64**, 1009 (2014).
9. S. A. Grigoriev, "Electrochemical systems with a solid polymer electrolyte. part ii. water electrolyzers, bifunctional elements, and hydrogen concentrators*." *Chemical and Petroleum Engineering*, **48**, 535 (2013).
10. P. Trinke, P. Haug, J. Brauns, B. Bensmann, R. Hanke-Rauschenbach, and T. Turek, "Hydrogen crossover in pem and alkaline water electrolysis: Mechanisms, direct comparison and mitigation strategies." *J. Electrochem. Soc.*, **165**, F502 (2018).
11. G. Tjarks, A. Gibelhaus, F. Lanzerath, M. Müller, A. Bardow, and D. Stolten, "Energetically-optimal pem electrolyzer pressure in power-to-gas plants." *Applied Energy*, **218**, 192 (2018).
12. M. Suermann, T. Kiupel, T. J. Schmidt, and F. N. Büchi, "Electrochemical hydrogen compression: Efficient pressurization concept derived from an energetic evaluation." *J. Electrochem. Soc.*, **164**, F1187 (2017).
13. S. A. Grigor'ev, M. M. Khaliullin, N. V. Kuleshov, and V. N. Fateev, "Electrolysis of water in a system with a solid polymer electrolyte at elevated pressure." *Russian Journal of Electrochemistry*, **37**, 819 (2001).
14. B. L. Kee, D. Curran, H. Zhu, R. J. Braun, S. C. DeCaluwe, R. J. Kee, and S. Ricote, "Thermodynamic insights for electrochemical hydrogen compression with proton-conducting membranes." *Membranes*, **9**, 77 (2019).
15. J. O. Bockris, A. K. N. Reddy, and M. Gamboa-Aldeco, *Modern Electrochemistry 2A: Fundamentals of Electrodics* (Kluwer Academic Publishers, Boston, MA) 2nd ed. (2002).
16. K. C. Neyerlin, W. Gu, J. Jorne, and H. A. Gasteiger, "Study of the exchange current density for the hydrogen oxidation and evolution reactions." *J. Electrochem. Soc.*, **154**, B631 (2007).
17. T. E. Springer, T. A. Zawodzinski, and S. Gottesfeld, "Polymer electrolyte fuel cell model." *J. Electrochem. Soc.*, **138**, 2334 (1991).
18. M. Suermann, T. J. Schmidt, and F. N. Büchi, "Cell performance determining parameters in high pressure water electrolysis." *Electrochimica Acta*, **211**, 989 (2016).
19. U. Babic, M. Suermann, F. N. Büchi, L. Gubler, and T. J. Schmidt, "Review–identifying critical gaps for polymer electrolyte water electrolysis development." *J. Electrochem. Soc.*, **164**, F387 (2017).
20. K. Ayers, N. Danilovic, R. Ouimet, M. Carmo, B. Pivovar, and M. Bornstein, "Perspectives on low-temperature electrolysis and potential for renewable hydrogen at scale." *Annual Review of Chemical and Biomolecular Engineering*, **10**, 219 (2019).
21. F. Ausfelder and A. Bazzanella, "Hydrogen in the chemical industry." *Hydrogen Science and Engineering : Materials, Processes, Systems and Technology*, ed. P. D. Stolten and D. B. Emonts (Wiley-VCH Verlag GmbH & Co. KGaA, Weinheim, Germany) Vol. 2, p. 19 (2016).
22. U. Eberle, B. Müller, and R. von Helmolt, "Fuel cell electric vehicles and hydrogen infrastructure: status 2012." *Energy & Environmental Science*, **5**, 8780 (2012).
23. T. Smolinka, N. Wiebe, P. Sterchele, A. Palzer, F. Lehner, M. Jansen, S. Kiemel, R. Miehe, S. Wahren, and F. Zimmermann, *Studie IndWEDe: Industrialisierung der Wasserelektrolyse in Deutschland: Chancen und Herausforderungen für nachhaltigen Wasserstoff für Verkehr, Strom und Wärme* (NOW-GmbH, Ed., Berlin) (2018).
24. Q. Feng, X.-Z. Yuan, G. Liu, B. Wei, Z. Zhang, H. Li, and H. Wang, "A review of proton exchange membrane water electrolysis on degradation mechanisms and mitigation strategies." *Journal of Power Sources*, **366**, 33 (2017).
25. A. Kusoglu and A. Z. Weber, "New insights into perfluorinated sulfonic-acid ionomers." *Chem. Rev.*, **117**, 987 (2017).
26. C. K. Mittelsteadt and J. A. Staser, "Electrolyzer membranes." *Polymer Science: A Comprehensive Reference*, ed. K. Matyjaszewski and M. Möller (Elsevier, Amsterdam) p. 849 (2012).
27. T. Schuler, J. M. Ciccone, B. Krentscher, F. Marone, C. Peter, T. J. Schmidt, and F. N. Büchi, "Hierarchically structured porous transport layers for polymer electrolyte water electrolysis." *Adv. Energy Mater.*, **10**, 1903216 (2020).
28. National Institute of Standards and Technology, (2020), Chemisty Webbook U.S. Department of Commerce Ed. [Online]. Available: https://webbook.nist.gov/chemistry/form-ser/.
29. J. Zheng, X. Zhang, P. Xu, C. Gu, B. Wu, and Y. Hou, "Standardized equation for hydrogen gas compressibility factor for fuel consumption applications." *International Journal of Hydrogen Energy*, **41**, 6610 (2016).
30. W. Wagner and H.-J. Kretzschmar, *International steam tables: Properties of water and steam based on the industrial formulation IAPWS-IF97* (Springer, Berlin) 2nd ed. (2008).
31. M. Suermann, T. J. Schmidt, and F. N. Büchi, "Comparing the kinetic activation energy of the oxygen evolution and reduction reactions." *Electrochimica Acta*, **281**, 466 (2018).
32. J. Durst, C. Simon, F. Hasché, and H. A. Gasteiger, "Hydrogen oxidation and evolution reaction kinetics on carbon supported pt, ir, rh, and pd electrocatalysts in acidic media." *J. Electrochem. Soc.*, **162**, F190 (2015).
33. M. Bernt and H. A. Gasteiger, "Influence of ionomer content in iro 2 /tio 2 electrodes on pem water electrolyzer performance." *J. Electrochem. Soc.*, **163**, F3179 (2016).
34. P. Trinke, G. P. Keeley, M. Carmo, B. Bensmann, and R. Hanke-Rauschenbach, "Elucidating the effect of mass transport resistances on hydrogen crossover and cell performance in pem water electrolyzers by varying the cathode ionomer content." *J. Electrochem. Soc.*, **166**, F465 (2019).
35. R. Battino, R. Cargill, C. Chen, H. Clever, and J. Roth, "Oxygen and Ozone." *Solubility Data Series* (International union of pure and applied chemistry, Ed.) (1981).
36. D. L. Wise and G. Houghton, "The diffusion coefficients of ten slightly soluble gases in water at 10–60 °C." *Chemical Engineering Science*, **21**, 999 (1966).
37. C. Young, R. Battino, H. Clever, and D. Wiesenburg, "Hydrogen and Deuterium." *Solubility Data Series* (International union of pure and applied chemistry, Ed.) (1981).
38. P. Trinke, B. Bensmann, S. Reichstein, R. Hanke-Rauschenbach, and K. Sundmacher, "Hydrogen permeation in pem electrolyzer cells operated at asymmetric pressure conditions." *J. Electrochem. Soc.*, **163**, F3164 (2016).
39. F. B. Spingler, A. Phillips, T. Schuler, M. C. Tucker, and A. Z. Weber, "Investigating fuel-cell transport limitations using hydrogen limiting current." *International Journal of Hydrogen Energy*, **42**, 13960 (2017).
40. C. Czeslik, H. Seemann, and R. Winter, "Basiswissen Physikalische Chemie." *Vieweg+Teubner Verlag/GWV Fachverlage GmbH Wiesbaden*, **4**, 77 (2010).
41. P. Choi, D. G. Bessarabov, and R. Datta, "A simple model for solid polymer electrolyte (spe) water electrolysis." *Solid State Ionics*, **175**, 535 (2004).
42. R. García-Valverde, N. Espinosa, and A. Urbina, "Simple pem water electrolyser model and experimental validation." *International Journal of Hydrogen Energy*, **37**, 1927 (2012).
43. P. Trinke, B. Bensmann, and R. Hanke-Rauschenbach, "Current density effect on hydrogen permeation in pem water electrolyzers." *International Journal of Hydrogen Energy*, **42**, 14355 (2017).
44. P. Trinke, B. Bensmann, and R. Hanke-Rauschenbach, "Experimental evidence of increasing oxygen crossover with increasing current density during pem water electrolysis." *Electrochemistry Communications*, **82**, 98 (2017).
45. B. Tjaden, S. J. Cooper, D. J. L. Brett, D. Kramer, and P. R. Shearing, "On the origin and application of the bruggeman correlation for analysing transport phenomena in electrochemical systems." *Current Opinion in Chemical Engineering*, **12**, 44 (2016).
46. J. Fimrite, B. Carnes, H. Struchtrup, and N. Djilali, "Transport phenomena in polymer electrolyte membranes." *J. Electrochem. Soc.*, **152**, A1815 (2005).
47. H. Ito, N. Miyazaki, M. Ishida, and A. Nakano, "Cross-permeation and consumption of hydrogen during proton exchange membrane electrolysis." *International Journal of Hydrogen Energy*, **41**, 20439 (2016).
48. F. N. Büchi and G. G. Scherer, "Investigation of the transversal water profile in nafion membranes in polymer electrolyte fuel cells." *Solid State Ionics*, **148**, A183 (2001).